Sandia National Laboratories

Graphite Steel and Chromium-Nickel Steel Corrosion: Solution Flow-Through Corrosion Experiments

Prepared by:

Charlotte Sisk-Scott

Cassandra Marrs

Repository Performance Dept. 8882

Sandia National Laboratories

Carlsbad, NM

TABLE OF CONTENTS

| 1.0 Introduction | 7 |
|------------------------------------------------------------------------------------------------|----|
| 2.0 Experimental Approach and Methods | 8 |
| 3.0 Determination of Surface Retreat Rates by Total Fe (Fe _τ) Concentration | 11 |
| 4.0 Determination of Corrosion Rates by Mass Loss | 18 |
| 5.0 Determination of Corrosion Rates by 3-D Interferometry | 24 |
| 6.0 Identification of Corrosion Products by Raman Spectroscopy | 34 |
| 7.0 Uncertainty Determination | 38 |
| 8.0 Conclusions | 40 |
| 9.0 References | 44 |

LIST OF TABLES

| Table 1 Experimental Parameters 8 |
|---------------------------------------------------------------------------------------|
| Table 2 Solution 3 Brine Composition |
| Table 3 Composition of Graphite steel Coupons (KIT-F1,-F2,-F3) 9 |
| Table 4 Composition of Cr-Ni Coupons (KIT-F4,-F5,-F6) 9 |
| Table 5. Coupon dimensions, mass and calculated densities for the flow-through |
| experiments |
| Table 6. Mean, minimum, and maximum concentrations of elements in samples from |
| Graphite steel and Cr-Ni steel corrosion tests as determined by ICP-MS and ICP- |
| OES |
| Table 7 Total Fe Concentration Surface Retreat Rates for Samples |
| Table 8 Chemical Cleaning Procedures for Coupons 19 |
| Table 9 Mass Loss Corrosion Rates for Samples. 24 |
| Table 10 Interferometer Corrosion Rates for Samples 34 |
| Table 11 Average corrosion rates for KIT graphite steel and Cr-Ni steel coupons based |
| on Fe_{τ} , mass loss, and interferometry results |

LIST OF FIGURES

| Figure 1. Release amounts of Fe and Si from graphite steel (KIT-F1) in 5 M NaCl |
|-------------------------------------------------------------------------------------------------------|
| brine14 |
| Figure 2. Release amounts of Fe and Si from graphite steel (KIT-F2) in 3.4 M MgCl ₂ |
| brine14 |
| Figure 3. Release amounts of Fe and Si from graphite steel (KIT-F3) in Solution 3 |
| brine |
| Figure 4. Release amounts of Fe, Si, Cr, and Ni from Cr-Ni steel (KIT-F4) in 5 M |
| NaCl brine |
| Figure 5. Release amounts of Fe, Si, Cr, and Ni from Cr-Ni steel (KIT-F5) in 3.4 M |
| MgCl ₂ brine |
| Figure 6. Release amounts of Fe, Si, Cr, and Ni from Cr-Ni steel (KIT-F6) in Solution |
| 3 brine |
| Figure 7. Graphical method used to determine coupon mass loss for KIT-F1 sample. |
| True mass of the specimen after removal of the corrosion products will be the |
| extrapolated y-intercept value at point D |
| Figure 8. Graphical method used to determine coupon mass loss for KIT-F2 sample. |
| True mass of the specimen after removal of the corrosion products will be the |
| extrapolated y-intercept value at point D |
| Figure 9. Graphical method used to determine coupon mass loss for KIT-F3 sample. |
| True mass of the specimen after removal of the corrosion products will be the |
| extrapolated y-intercept value at point D |

| Figure 10. Graphical method used to determine coupon mass loss for KIT-F4 sample. |
|-------------------------------------------------------------------------------------------|
| True mass of the specimen after removal of the corrosion products will be the |
| extrapolated y-intercept value at point D |
| Figure 11. Graphical method used to determine coupon mass loss for KIT-F5 sample. |
| True mass of the specimen after removal of the corrosion products will be the |
| extrapolated y-intercept value at point D |
| Figure 12. Graphical method used to determine coupon mass loss for KIT-F6 sample. |
| True mass of the specimen after removal of the corrosion products will be the |
| extrapolated y-intercept value at point D |
| Figure 13. A cartoon illustrating the interferometry strategy |
| Figure 14. Photographs of post-experiment graphite steel coupons |
| Figure 15. Photographs of post-experiment Cr-Ni steel coupons |
| Figure 16. Interferometer image of a polished coupon surface before it was subjected |
| to aqueous corrosion29 |
| Figure 17. 3-D interferometric image of the graphite steel coupon, KIT-F1, after |
| exposure to 5 M NaCl for 160 days. The surface shows evidence of extensive |
| roughening30 |
| Figure 18. 3-D interferometric image of the graphite steel coupon, KIT-F2, after |
| exposure to 3.4 M MgCl ₂ for 160 days. The surface shows evidence of extensive |
| roughening and pitting30 |
| Figure 19. 3-D interferometric image of the graphite steel coupon, KIT-F3, after |
| exposure to Soln. 3 for 160 days. The surface shows evidence of extensive |
| roughening31 |

| Figure 20. 3-D interferometric image of the Cr-Ni steel coupon, KIT-F4, after |
|-------------------------------------------------------------------------------------------------------|
| exposure to 5 M NaCl for 160 days. The surface shows little evidence of surface |
| roughening32 |
| Figure 21. 3-D interferometric image of the Cr-Ni steel coupon, KIT-F5, after |
| exposure to 3.4 M MgCl ₂ for 160 days. The surface shows little evidence of |
| surface roughening |
| Figure 22. 3-D interferometric image of the Cr-Ni steel coupon, KIT-F6, after |
| exposure to Soln. 3 for 160 days. The surface shows little evidence of surface |
| roughening |
| Figure 23. Raman spectrum of magnetite + GR detected on Coupon KIT-F1 from |
| flow through experiments in 5 M NaCl brine |
| Figure 24. Raman spectrum of GR detected on Coupon KIT-F2 from flow through |
| experiments in 3.4 M MgCl ₂ brine |
| Figure 25. Raman spectrum of GR + akageneite + goethite detected on Coupon KIT- |
| F3 from flow through experiments in Solution 3 brine |
| Figure 26. Graphite steel coupon corrosion rates using Total iron (Fe $_{\tau}$), mass loss, and |
| interferometry techniques41 |
| Figure 27. Cr-Ni steel coupon corrosion rates using Total iron (Fe $_{\tau}$), mass loss, and |
| interferometry techniques 41 |

1.0 Introduction

The corrosion of steel, when exposed to various compositions of brines is a complex, heterogeneous process involving dissolution and precipitation of multiple solids. The rate at which elements will be released from the corrosion process under these conditions will depend, in part, on effects associated with secondary alteration phases (passivating film) that may potentially form under these conditions. Understanding these processes has required the development of sophisticated methods to sample and quantitatively characterize the composition of the steel as it corrodes and releases elements. The determination of the concentrations of both brine and steel corrosion components in solutions sampled from these tests is required to fully understand the process that may eventually lead to dissolution of corrosion products.

Inductively coupled plasma mass spectrometry (ICP-MS) and inductively coupled plasma optical emission spectrometry (ICP-OES) are well suited for these analyses. However, low solubility of elements in brines frequently results in concentrations below detection limits (DL) of many important elements (e.g. DL Fe=5ppb; DL Si=20ppb; and DL Ni= 0.05ppb), particularly after the formation of secondary alteration phases on the carrion surface.

The purpose of this report is to quantify the steel corrosion rates as a function of dissolved chloride and metal concentration. The experiments are configured as a Single-Pass Flow-Through (SPFT) set-up as described in Test Plan 06-02 (Sisk-Scott et al., 2016). Using ICP-MS/ICP-OES, mass loss data, and 3-D interferometry height profile results, the experiments will provide a comprehensive understanding of the metal corrosion process that cannot be obtained individually. In each of these sections, the experiments are described and how data, especially corrosion rate data, are obtained.

2.0 Experimental Approach and Methods

Steel corrosion tests are being performed for Karlsruhe Institute of Technology (KIT) on a suite of coupons under a variety of experimental configurations designed to simulate geologically saturated brine and anoxic conditions. Both Chromium-Nickel (Cr-Ni) steel and Graphite steel coupons are being studied. The configurations consist of the following components and concentrations of brines.

 Table 1 Experimental Parameters

| Sample ID | Brine Solution | Coupon Composition |
|-----------|-----------------------|--------------------|
| KIT-F1 | 5 M NaCl | Graphite steel |
| KIT-F2 | $3.4~\mathrm{MgCl_2}$ | Graphite steel |
| KIT-F3 | Solution 3 | Graphite steel |
| KIT-F4 | 5 M NaCl | Cr-Ni steel |
| KIT-F5 | $3.4~\mathrm{MgCl_2}$ | Cr-Ni steel |
| KIT-F6 | Solution 3 | Cr-Ni steel |

Table 2 Solution 3 Brine Composition

| Chemical Composition | |
|-----------------------------------------------|------------------------------------------------------------------------------------------------------------------------------------------|
| 5 M NaCl | |
| 0.0188 M CaCl ₂ •2H ₂ O | |
| 0.0188 M Na ₂ SO ₄ | |
| $0.015~\mathrm{M~K_2SO_4}$ | |
| 0.015 M MgSO ₄ •7H ₂ O | |
| | 5 M NaCl 0.0188 M CaCl ₂ •2H ₂ O 0.0188 M Na ₂ SO ₄ 0.015 M K ₂ SO ₄ |

The certified composition of the coupons is given in Tables 3 and 4. The coupons are approximately $3 \times 49 \times 49$ mm.

Table 3 Composition of Graphite steel Coupons (KIT-F1,-F2,-F3)

| Element | Weight Percent |
|---------|----------------|
| С | 3.46 |
| Cr | 0.042 |
| Cu | 0.037 |
| Fe | balance |
| Mn | 0.29 |
| P | 0.035 |
| Si | 0.010 |
| S | 0.0024 |
| Mg | 0.052 |

Source: Mittelrheinische Metallgießerei Heinrich Beyer GmbH & Co. KG

Table 4 Composition of Cr-Ni Coupons (KIT-F4,-F5,-F6)

| Element | Weight Percent |
|---------|----------------|
| С | 0.061 |
| Cr | 22.45 |
| Cu | 0.230 |
| Fe | 62.5 |
| Mn | 1.15 |
| N | 0.027 |
| Ni | 13.17 |
| P | 0.023 |
| Si | 0.35 |
| S | 0.001 |
| Mo | 0.23 |
| | |

Source: thyssenkrupp accial speciali terni spa

Six solutions were prepared for the SPFT experiments. Solutions 1-6 are described in Tables 1 and 2.

The deionized water was transferred inside the glovebox and each liter of water was purged inside the glovebox for a minimum of two hours. ACS grade or better chemicals were supplied by approved vendors. The chemicals were all weighed outside of the glovebox and then transferred into the glovebox. All balances were calibrated prior to use. Once all the water was purged and the solids were weighed, the solutions were prepared inside the glovebox. All solutions were made 1-L at a time with the water being weighed inside the glovebox to make sure the purged water remained free of oxygen and carbonates. Solutions were then added to intravenous (IV) bags. Replacement solutions were made as needed using the same procedure.

The metal coupons were polished to a mirror finish prior to being placed directly in the process stream and only extracted upon termination of the experiment. The coupons were housed in a 120 mL Savillex Teflon digestion vessel into which the simulated brines are continuously injected via a peristaltic pump at an injection rate of 60 mL/d. Coupons are contained in the holder assembly so that the brine contacts the coupon, percolates over the sample, and is collected in the bottom of a sample tube. The holder assemblies are contained in an aluminum casing specifically designed to be heated by a heater block held typically at $90\pm2^{\circ}$ C. The experiments were carried out in a double, four-port OMNI-Lab (Vacuum Atmospheres Company) inert atmosphere glovebox that contained a Cu-based catalytic oxygen scrubber. Frequent regeneration of the Cu-catalyst using a N_2 -H₂ mixture coupled with judicious sparging with ultrapure N_2 decreased oxygen concentrations to $0.2 < O_2 < 0.4$ ppmv. Tests were continuously run and samples intermittently taken approximately weekly so that the reaction process could be observed. At these times alteration phases could be sampled, and the leachate

was collected for analysis. After collection of the leachate, the sample was acidified with 2% HNO₃ for sample analyses. The acidified leachate was analyzed by ICP-MS or ICP-OES. These tests have been sampled 22 times at approximately 23 weeks of reaction.

3.0 Determination of Surface Retreat Rates by Total Fe (Fe₇) Concentration

Unlike other methods, the SPFT test can maintain constant experimental conditions due to the continual replenishment of solution from reservoirs through the reactor therefore sweeping out elements released from the coupon to the effluent. Accordingly, the best way to compare the rates of different experiments conducted under different conditions (temperature, solution composition) is to run experiments under the same flow-rate to sample surface area ratio. With the demonstration of steady-state rates, the experimental activation energy can be determined more accurately.

The dissolution rate of steel can be determined from:

$$-r_j = \frac{(c_{i,in} - c_{i,out}) * f_{s,j}}{v_i \times A_{s,j}}$$
[1]

where r_j is the mass flux of an element at time j [g/(m²·d)], $C_{i,in}$ is the concentration of element i into the reactor (the "background" concentration; g/L), $C_{i,out}$ is the concentration of element i in the effluent (g/L), $f_{s,j}$ is the flow rate of effluent at time j (L/d), v_i is the mass fraction of element i in the steel coupon (dimensionless), and $A_{s,j}$ is the area of the coupon at time j (m²). By convention, the dissolution reaction is designated as a negative rate (hence the minus sign). The corrosion rate (μ m/yr) of the steel monolith can be computed by dividing the mass flux of Fe [Eq. (1)] by the density of steel seen in Table 5.

Table 5. Coupon dimensions, mass and calculated densities for the flow-through experiments.

| Coupon I.D. | KIT-F1 | KIT-F2 | KIT-F3 | KIT-F4 | KIT-F5 | KIT-F6 |
|---------------------------------|--------|--------|--------|--------|--------|--------|
| Surface area (cm ²) | 53.40 | 53.37 | 53.04 | 53.44 | 53.47 | 53.58 |
| Mass (g) | 71.53 | 70.84 | 71.91 | 79.74 | 79.95 | 80.41 |
| Density (g/cm ³) | 10.21 | 10.03 | 10.12 | 11.20 | 11.16 | 11.17 |

The ICP-MS analyses were performed on a Perkin Elmer NexION 8300 Dual View series ICP-MS instrument. The ICP-OES analyses were performed on a Perkin Elmer Optima 3000 series ICP-OES instrument. Because of the wide range of concentrations of brine and steel components in corrosion leachates, samples are typically analyzed in two procedures using two separate aliquots. In the first procedure, the heavier elements (Cr, Ni, Fe) are determined by ICP-MS. These analyses were performed on a 0.1-ml aliquot of leachate that has been diluted to a volume of 10 ml and spiked with a mixed internal standard containing Ge, Sc, In, Li, Tb, Y, and Bi. In the second procedure, the lighter element (Si) is determined by ICP-OES. These analyses were performed on the diluted leachate, spiked with a mixed internal standard containing Sc.

Samples were analyzed weekly, with a cumulative sum of 22 weeks of sampling. The mean, minimum, and maximum concentrations of elements in leachates solutions from the duration of the 22-week samplings are given in Table 6.

Table 6. Mean, minimum, and maximum concentrations of elements in samples from Graphite steel and Cr-Ni steel corrosion tests as determined by ICP-MS and ICP-OES.

| Mean Concentration (ppb) | | | Min-Max Concentration (ppb) | | | | | |
|--------------------------|-------|-------|-----------------------------|------|-------------|------------|------|--------|
| Species | Fe | Si | Cr | Ni | Fe | Si | Cr | Ni |
| KIT-F1 | 190 | 3070 | N/A | N/A | 7-836 | 2188-4083 | N/A | N/A |
| KIT-F2 | 27557 | 6418 | N/A | N/A | 16314-62262 | 5396-7644 | N/A | N/A |
| KIT-F3 | 785 | 2519 | N/A | N/A | 60-5482 | 1194-3317 | N/A | N/A |
| KIT-F4 | 57.6 | 2877 | 16.5 | 1.67 | 9-208 | 1960-4002 | 5-30 | 0.5-4 |
| KIT-F5 | 113 | 10650 | 30.6 | 44.4 | 50-483 | 8376-13660 | 6-90 | 2-147 |
| KIT-F6 | 52.5 | 2703 | 26.2 | 2.68 | 34-86 | 2116-3728 | 6-66 | 0.6-11 |

The results in Table 6 indicate that the Cr-Ni steel coupons (KIT-F4, -5, -F6) resulted in sparse concentrations of elemental Cr, Ni, and Fe. This is consistent with the lack of corrosion product found on the coupons when experiments were terminated, and coupons were removed from solution. This is not the case for the graphite steel coupons (KIT-F1, -F2, -F3), in which, Fe and Si have a high rate of dissolution. The dissolution of Si was high in all samples.

Kinetically, the dissolution of minerals is controlled by either transport or chemical reactions (hydration, hydrolysis, ion exchange, or redox reactions) at the interface of the steel and the solution. The protective passivation mechanisms can change over time as conditions change and the alteration layers evolve. The alteration films are amorphous, which means that they are thermodynamically unstable and can, according to the Ostwald rule of stages, dissolve, ripen, or crystallize, as observed by Crovisier (2003) leading to declines and increases in elemental concentrations. The crystallization of secondary phases also occurs through direct precipitation from solution. These processes can both occur progressively if crystallization is kinetically slow. Such a phenomenon can result in the loss of any protective properties of the interfacial layer and change the geochemical properties of the solution in contact with the coupon, either of which in turn can lead to accelerated dissolution rate.

In Figures 1-3, the concentration of Si is decreasing over time at an average change of rate of ~12 ppb/day. This could be due to the diminishing availability of soluble Si at the coupon interface, or the steady formation of an Fe build up on the surface during the active to passive corrosion transition. The decrease over time is not the case for Fe, in which the average change of rate ranged from ~4.4 ppb/day for KIT-F1 and KIT-F3 and 209 ppb/day for KIT-F2. The increase of Si dissolution in this domain suggests that Si builds up on the surface during the

active to passive corrosion transition and may play an important role in the passivation mechanism. The similar dissolution rate of change for the two coupons (KIT-F1 and KIT-F3) corresponds to similar surface retreat rates of 0.1 and 0.4 μ m/yr, as seen in Table 7. In both cases, there is a drop in total iron concentration (Fe_{τ}), which is indicative of a passivation film developing. The continuous decrease in Fe_{τ} changes for KIT-F3, in which a gradual increase is seen after 100 days. This trend is also seen for KIT-F2. The corresponding surface retreat rate by Fe_{τ} measurements for sample KIT-F2 is 15 μ m/yr.

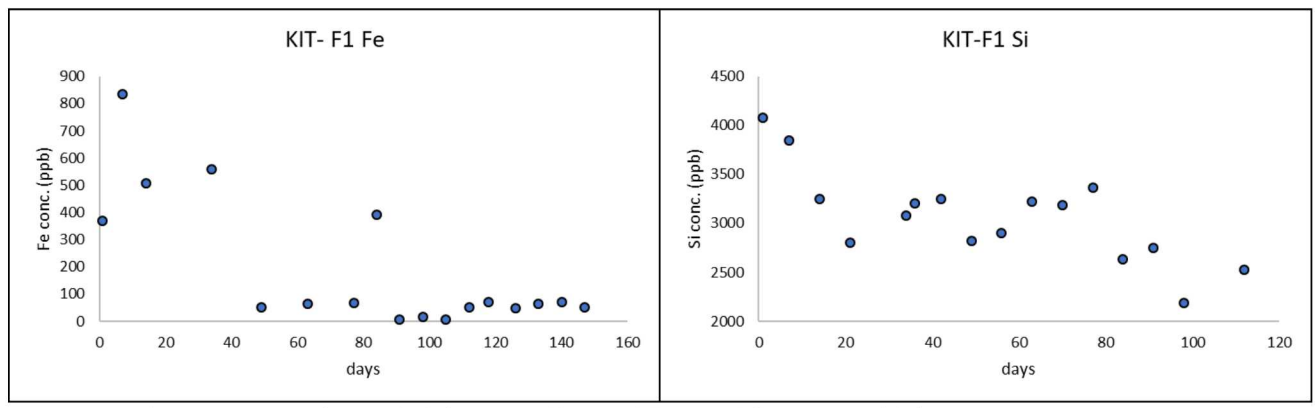


Figure 1. Release amounts of Fe and Si from graphite steel (KIT-F1) in 5 M NaCl brine.

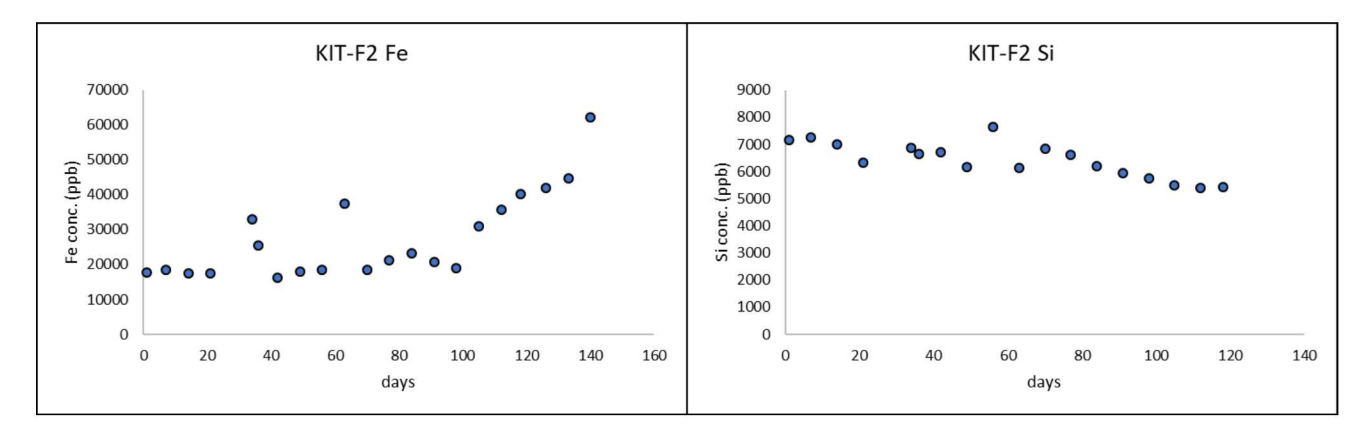


Figure 2. Release amounts of Fe and Si from graphite steel (KIT-F2) in 3.4 M MgCl₂ brine.

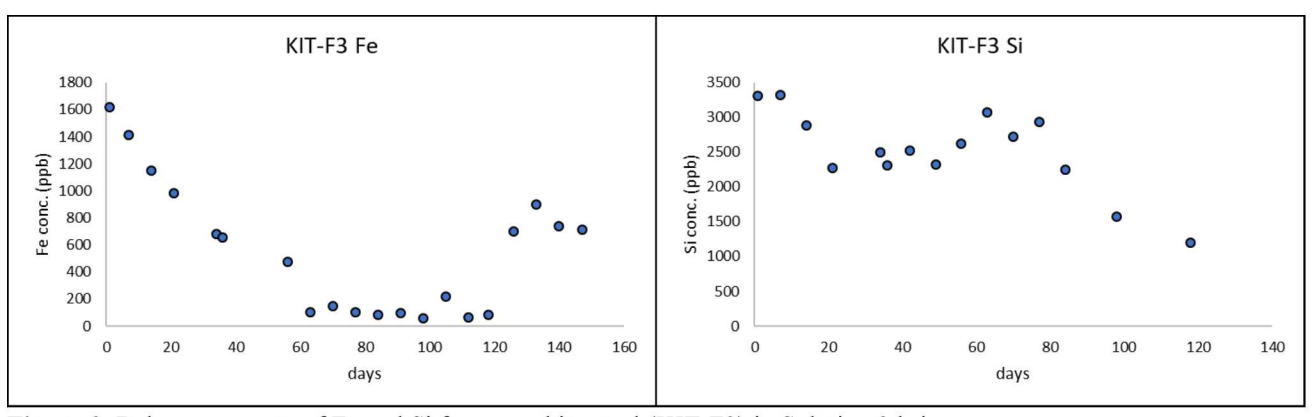


Figure 3. Release amounts of Fe and Si from graphite steel (KIT-F3) in Solution 3 brine.

The ion concentrations in the solution of Fe, Cr, Si, and Ni are shown in Figures 4-6 for samples KIT-F4, -F5, and -F6. Sample KIT-F4 exhibits no significant changes over time which would conclude that a passivation layer was not formed. There is a slight variation of concentration seen for KIT-F5. At approximately 80 days, Fe and Ni reveal an almost 150 ppb increase in concentration, but drastically drop back down again after 40 days. Whereas, sample KIT-F6 exhibits a slight increase in concentration over time for the Fe and Cr concentration. Metals react quickly with an exponential decrease in surface retreat rate as the passive film forms, eventually reaching a low steady state passive dissolution rate where the rate of metal oxidation and film formation at the metal/oxide interface equals the rate of film dissolution at the oxide/solution interface. The rate will then increase again if localized corrosion initiates.

Further characterization of corrosion products is needed in order to establish a trend in the results for the Cr-Ni steel samples.

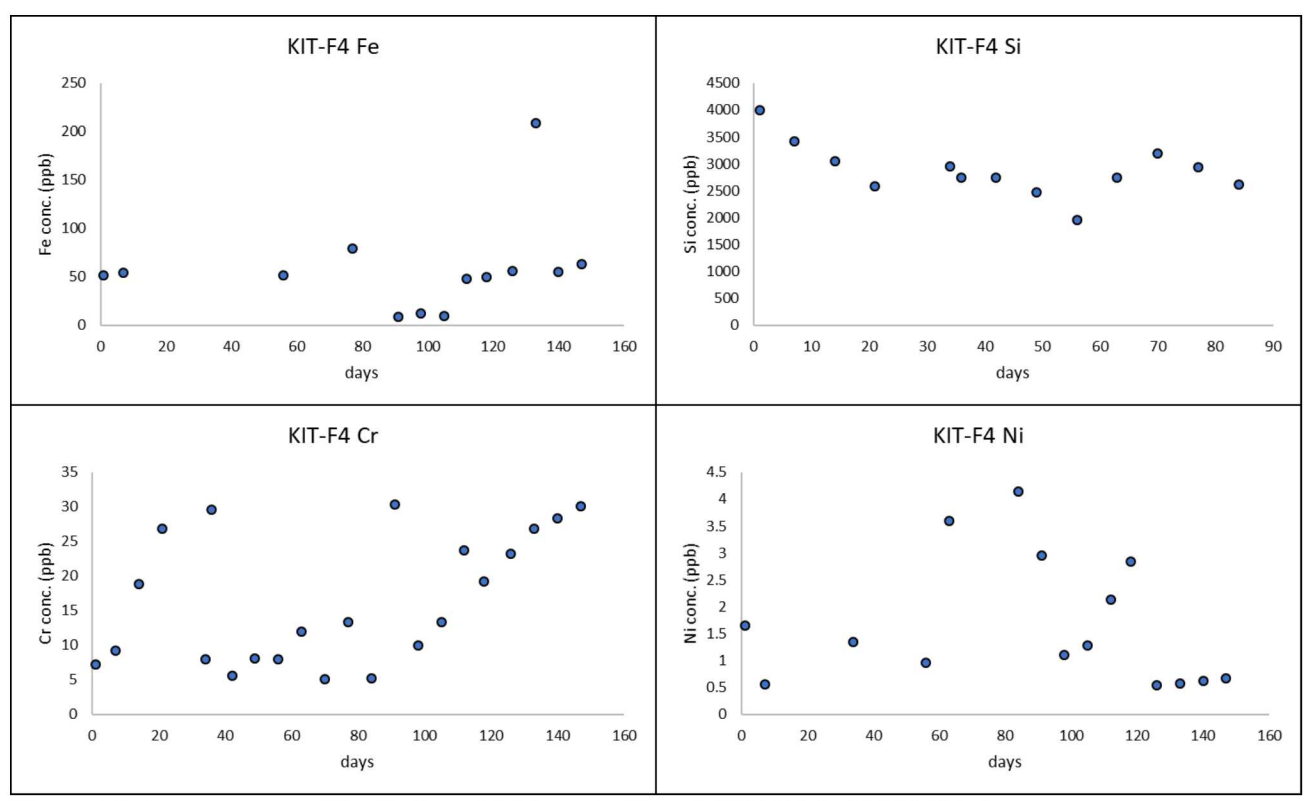


Figure 4. Release amounts of Fe, Si, Cr, and Ni from Cr-Ni steel (KIT-F4) in 5 M NaCl brine.

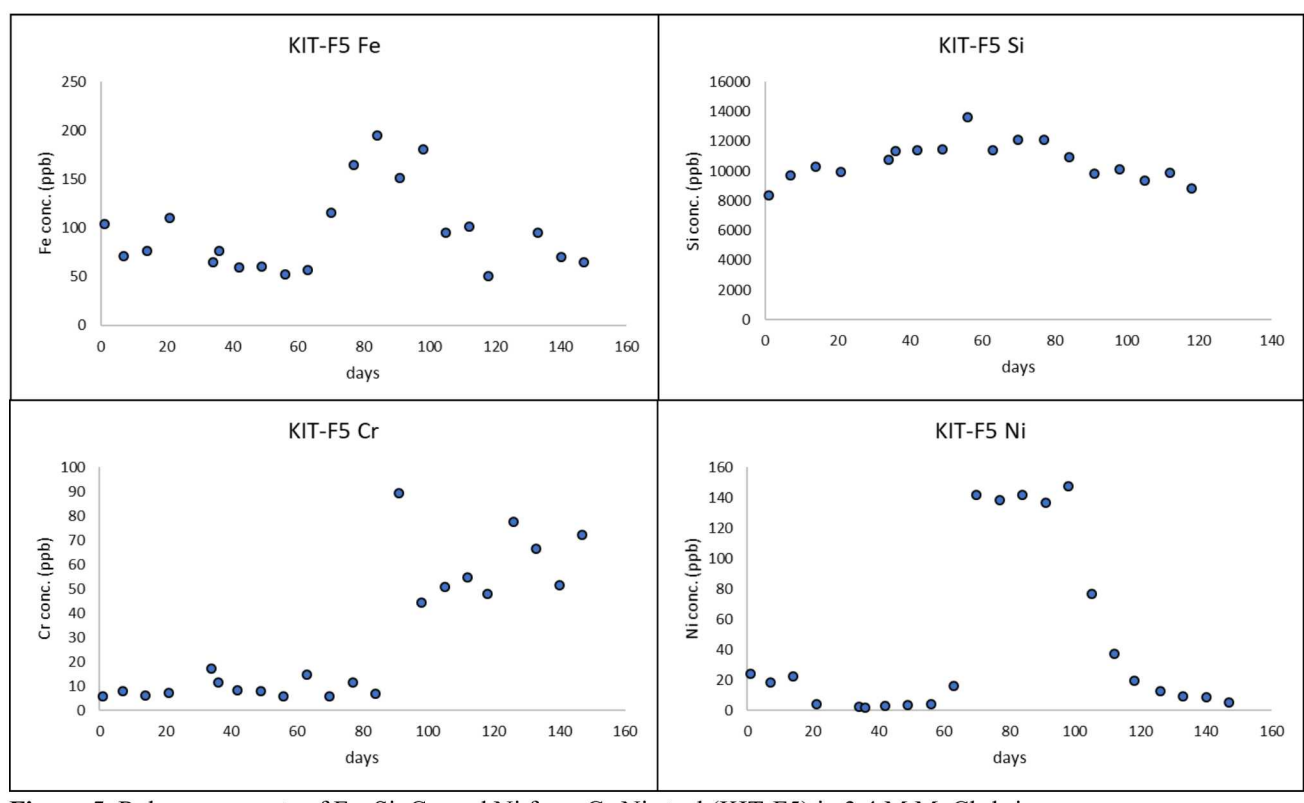


Figure 5. Release amounts of Fe, Si, Cr, and Ni from Cr-Ni steel (KIT-F5) in 3.4 M MgCl₂ brine.

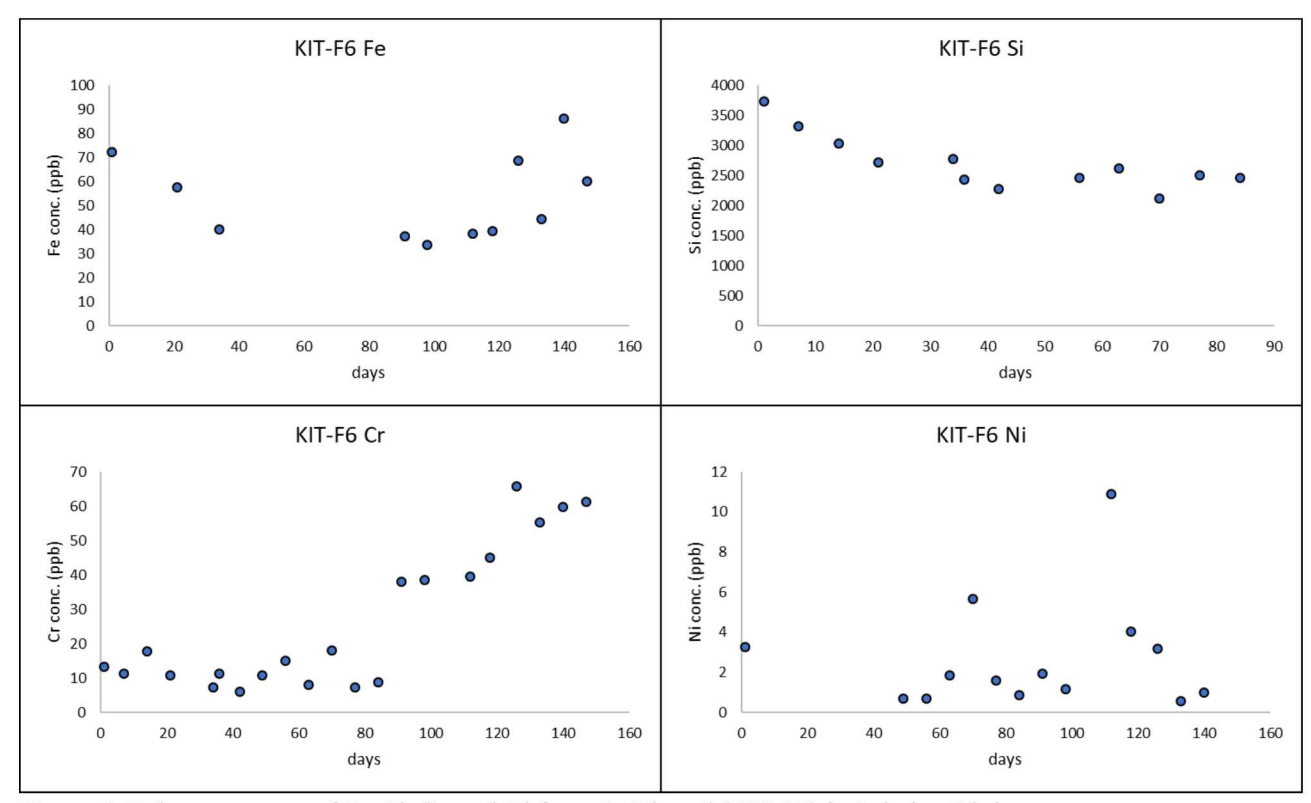


Figure 6. Release amounts of Fe, Si, Cr, and Ni from Cr-Ni steel (KIT-F6) in Solution 3 brine.

Concentrations of Fe, determined by the flow-rate, the surface area of the coupons, and the dissolution rates, with experimental uncertainties, are listed in Table 7. The corrosion rates of Cr-Ni steel coupons all resulted in low values (<0.1 µm/yr). Corrosion rates for graphite steel coupons reacted in MgCl₂ brine exhibited 10x higher rates compared to NaCl and solution 3 brines. Note, however, that the uncertainty on many of the values is as large as the value itself. These data attest to the significance of electrolytes and coupon composition in steel corrosion.

Table 7 Total Fe Concentration Surface Retreat Rates for Samples

| Sample ID | Chemical Composition | Brine | Corrosion Rate (µm/yr) | Corrosion Rate (g/(m ² d)) |
|-----------|----------------------|-------------------------|--------------------------|---------------------------------------|
| KIT-F1 | Graphite steel | 5.0 M NaCl | 0.10 ± 0.14 | 0.002 ± 0.003 |
| KIT-F2 | Graphite steel | 3.4 M MgCl ₂ | 14.98 ± 6.69 | 0.32 ± 0.14 |
| KIT-F3 | Graphite steel | Solution 3 | 0.43 ± 0.64 | 0.009 ± 0.014 |
| KIT-F4 | Cr-Ni steel | 5.0 M NaCl | 0.05 ± 0.04 | 0.001 ± 0.0009 |
| KIT-F5 | Cr-Ni steel | 3.4 M MgCl ₂ | $\textbf{0.09} \pm 0.07$ | 0.002 ± 0.002 |
| KIT-F6 | Cr-Ni steel | Solution 3 | 0.11 ± 0.23 | 0.002 ± 0.005 |

4.0 Determination of Corrosion Rates by Mass Loss

After the corrosion tests were completed, coupons for each test condition were chemically cleaned in order to remove all of the corrosion products. The mass of the coupons after cleaning is compared to the initial mass and the difference represents the loss of material to corrosion. The mass loss can then be used to calculate a corrosion rate.

There is a standard procedure that outlines requirements for the cleaning of corrosion samples: ASTM G 1–03. All coupons were cleaned per the requirements outlined in this standard. The cleaning process included multiple cycles of chemical etching, brushing with a nonmetallic soft bristle brush followed by rinsing with deionized water. Following each cleaning cycle, the coupons were dried and weighed. A minimum of five cleaning cycles were performed for each coupon. The details of the chemical cleaning solution used for are shown in Table 8.

 Table 8 Chemical Cleaning Procedures for Coupons

| Chemical | Time | Temperature |
|--------------------------------------|--------|-------------|
| 500 mL conc. Hydrochloric acid (HCl) | | |
| 3.5 g Hexamethylene Tetramine | 10 min | 20 to 25 °C |
| Reagent water to make 1000 mL | | |
| | | |

Source: ASTM G 1-03

Because the above cleaning procedure removes some amount of base metal in addition to the corrosion products a procedure needs to be employed that corrects the weight loss measurements for the base metal loss. This study uses a procedure of graphical analysis based on multiple cleaning cycles in order to extrapolate the actual weight loss due to corrosion from the total measured weight loss. The graphical analysis method is outlined in ISO 8407: 1991 and is shown schematically in Figures 7-12. The mass of a coupon should have a linear relationship with respect to the cleaning cycles as long as the duration of each cycle is the same. A plot of the mass versus cleaning cycles ideally results in two lines (AB and BC in Figures 7-12). Line AB characterizes the removal of corrosion products and minor amounts of base metal, whereas line BC is the result of removal of the base metal substrate after all corrosion products have been removed. Extrapolation of the linear trendline for C to the 0th cleaning cycle (point D) provides the true mass of the coupon without the corrosion products on the surface at zero cleaning cycles. For the purposes of determining mass loss in this study, point D is taken as the final weight.

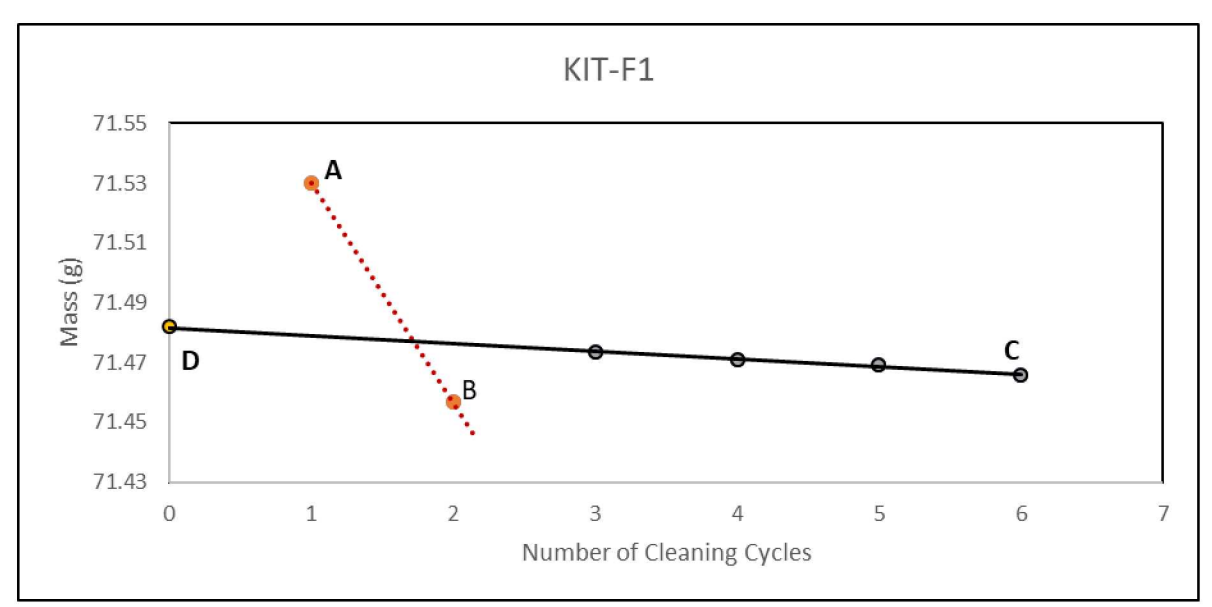


Figure 7. Graphical method used to determine coupon mass loss for KIT-F1 sample. True mass of the specimen after removal of the corrosion products will be the extrapolated y-intercept value at point D.

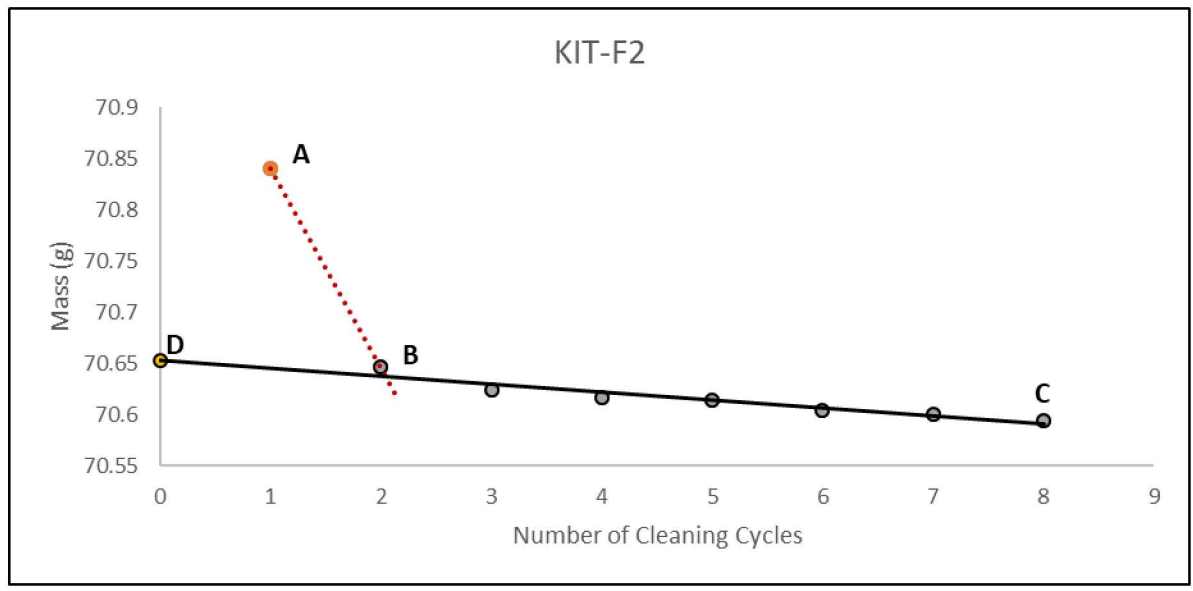


Figure 8. Graphical method used to determine coupon mass loss for KIT-F2 sample. True mass of the specimen after removal of the corrosion products will be the extrapolated y-intercept value at point D.

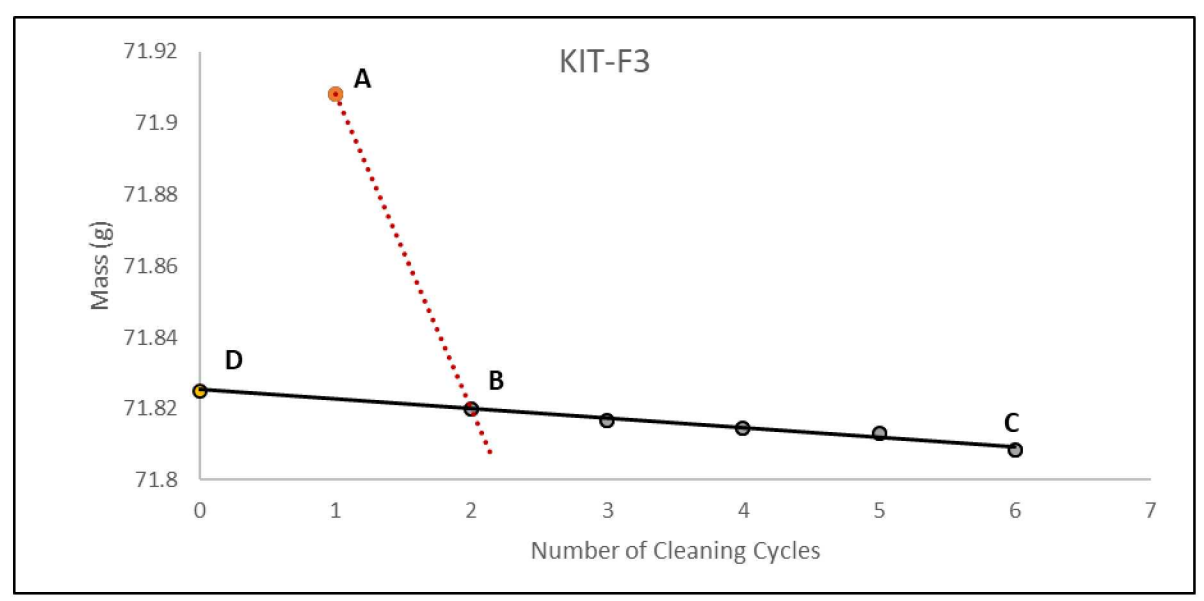


Figure 9. Graphical method used to determine coupon mass loss for KIT-F3 sample. True mass of the specimen after removal of the corrosion products will be the extrapolated y-intercept value at point D.

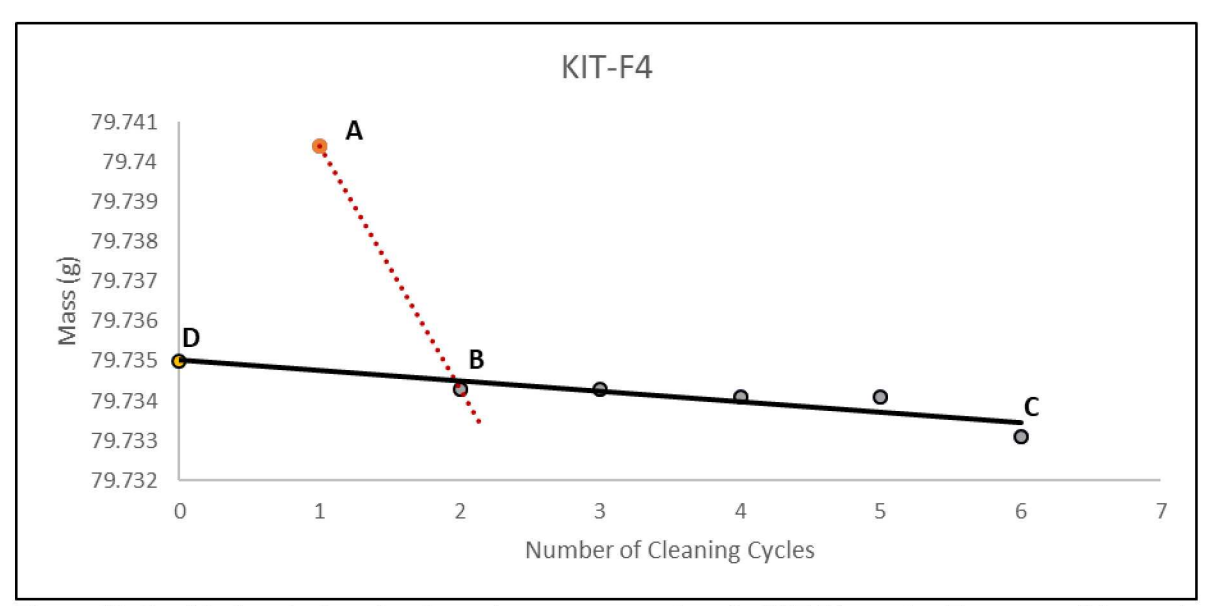


Figure 10. Graphical method used to determine coupon mass loss for KIT-F4 sample. True mass of the specimen after removal of the corrosion products will be the extrapolated y-intercept value at point D.

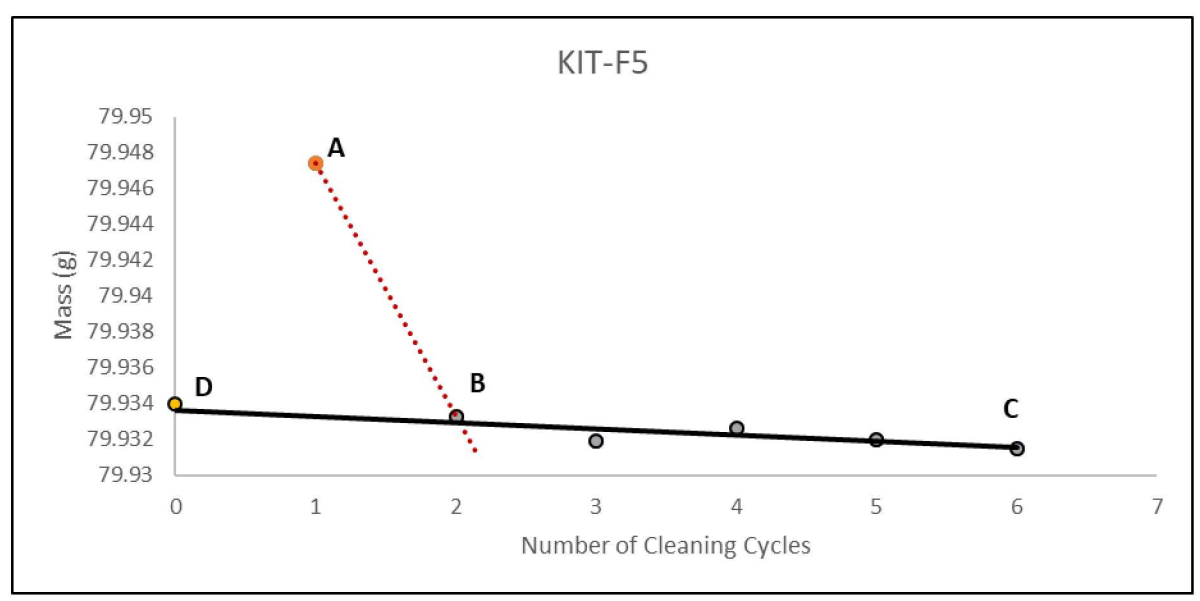


Figure 11. Graphical method used to determine coupon mass loss for KIT-F5 sample. True mass of the specimen after removal of the corrosion products will be the extrapolated y-intercept value at point D.

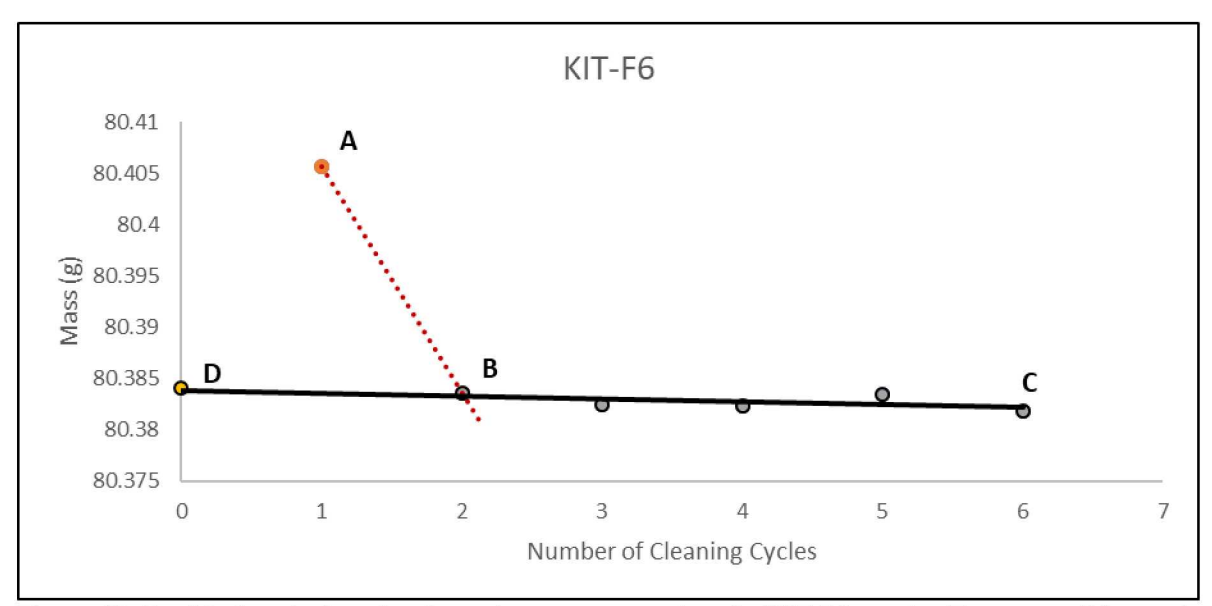


Figure 12. Graphical method used to determine coupon mass loss for KIT-F6 sample. True mass of the specimen after removal of the corrosion products will be the extrapolated y-intercept value at point D.

Corrosion rates are calculated from the mass loss data according to the following formula (NACE, 2000):

$$rate (r) = \frac{W \times 87.6}{SA \times t \times \rho} \times 1000$$
 [2]

where rate(r) is the corrosion rate in μ m/yr, W the mass loss (mg), SA the exposed surface area of the coupon (cm²), t the exposure duration (hours), ρ the metal density (g/cm³) and 1,000 converts the rate from mm/yr to μ m/yr.

Table 9 gives the coupon corrosion rates calculated from the weight-loss and surface area measurements for each chemical composition and brine type. In general, the rates determined by weight loss accorded reasonably well with the rates obtained through interferometry (Table 10). For example, the rates obtained by weight loss for experiments KIT-F1 and KIT-F3 are $2.0 - 3.5 \mu m/yr$ compared to $5.4 - 5.0 \mu m/yr$ by interferometry. In the case of KIT-F2, the rate determined by weight loss and interferometry were relatively fast (7.9 μm/yr and 10 μm/yr, respectively). In these two cases, the relatively fast rates appear to be the result of pitting that occurred in the high chloride solutions. Metal is removed from the surface as dissolved ions or corrosion products and swept from away from the metal surface. Pitting caused large chunks of steel to spall off the coupon surface, resulting in large corrosion rate values (15 μm/yr) by ICP-OES. The corrosion pits and spalled off areas lead to the removal or weakening of the protective film in the surrounding area and cause further pitting and spalling. This continuous process results in increased dissolution retreat due to the competing process of pitting and repassivation (Cruz et al., 1998). Relatively small corrosion rates were observed for the Cr-Ni coupons, ranging from 0.2-0.8 µm/yr.

Table 9 Mass Loss Corrosion Rates for Samples

| Sample ID | Chemical Composition | Brine | Corrosion Rate (µm/yr) | Corrosion Rate (g/(m ² d)) |
|-----------|----------------------|-------------------------|------------------------|---------------------------------------|
| KIT-F1 | Graphite steel | 5.0 M NaCl | 2.00 ± 0.26 | 0.056 ± 0.043 |
| KIT-F2 | Graphite steel | 3.4 M MgCl ₂ | 7.90 ± 0.62 | 0.218 ± 0.103 |
| KIT-F3 | Graphite steel | Solution 3 | 3.51 ± 0.29 | 0.098 ± 0.049 |
| KIT-F4 | Cr-Ni steel | 5.0 M NaCl | 0.20 ± 0.10 | 0.0063 ± 0.0169 |
| KIT-F5 | Cr-Ni steel | 3.4 M MgCl ₂ | 0.51 ± 0.11 | 0.016 ± 0.019 |
| KIT-F6 | Cr-Ni steel | Solution 3 | 0.82 ± 0.12 | 0.025 ± 0.020 |

5.0 Determination of Corrosion Rates by 3-D Interferometry

The drawback of determining steel corrosion rates by Fe release into effluent solution is that some of the iron released will reprecipitate on the monolith surface as corrosion products. Even though solution is constantly being replenished by fresh solution from the reservoir, effectively sweeping some aqueous Fe into the effluent collection vessel, some of the iron will still be retained as corrosion products. Thus, the measured rate will in most cases underestimate the true corrosion rate.

A problem with traditional methods of determining steel dissolution rates, such as by weight loss, is that pitting can take place on the steel surface, resulting in pieces of steel lifting off the surface and separating from the coupon. In such a scenario, the measured "weight loss" of the main coupon body is not indicative of dissolution and the pitting may not be representative of processes occurring at the steel surface.

The problems associated with the previously described corrosion rate measurements can be circumvented by measurement of the surface retreat rate over an area of the steel/solution

interface. This can be accomplished by using white light interferometry, in which minute vertical distances can be accurately measured. The strategy consists of polishing the steel monoliths to mirror finish and then adding small spots of Room Temperature Vulcanized (RTV) silicone sealant to the surface. The sealant protects the underlying surface from reaction with solution and preserves a reference surface. The monolith with its spots of sealant is then placed into a reactor. The monolith reacts with the solution flowing through the reactor and as the monolith dissolves, the surface retreats. After a certain amount of time has elapsed, the monolith can be extracted from the reactor and the sealant spots removed. Because a reference surface has been preserved, the absolute surface retreat can be measured using interferometry. The difference in height between the reference and reacted surfaces is proportional to the dissolution (flux) rate:

$$rate (r) = \frac{\Delta h}{\Delta t}$$
 [3]

where Δh is the height difference between the reference and reaction surfaces, and Δt is elapsed time. The rate is in units of μ m/y and is directly comparable to rates (fluxes) determined by Fe and mass loss measurements.

Because the circumference of the spot is on the millimeter scale, multiple measurements of the height difference between the reference and reaction surfaces can be performed on a single spot. Therefore, dozens to hundreds of height measurements can be made on the same monolith to obtain statistically significant rate values. The interferometry strategy is summarized in Figure 13A and an interferometric image is displayed in Figure 13B. See Icenhower and Steefel (2015) for a detailed discussion of this method.

A potential drawback of this method is that the reaction surface could be covered with corrosion products. Measurement of the height difference could therefore be compromised by a

layer of corrosion products on top of the reaction surface. To mitigate this effect, the monoliths were carefully cleaned in a solution according to Table 8 and as discussed in Sisk-Scott (2019). After 3 to 5 cleaning cycles, the corrosion products were removed.

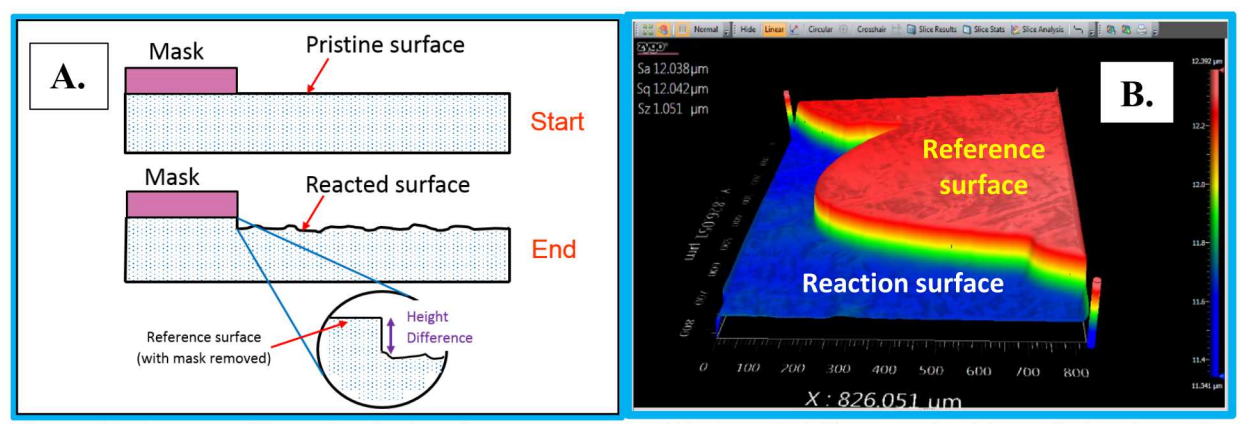


Figure 13. A cartoon illustrating the interferometry strategy (**A**). A mask (silicone sealant) is applied to the surface of a steel monolith (in cross section) and placed into a reactor. Solution reacts with the exposed surface of steel, causing dissolution and surface retreat. The monolith is then extracted from the reactor and the sealant mask removed, revealing a pristine reference surface. The difference in height between the reference and reaction surface is proportional to the dissolution (flux) rate. An actual interferometric image of a reference and reaction surface on a monolith of glass that was reacted in a flow-through reactor, like that used in the steel corrosion experiments (**B**).

A NewView 8300 (Zygo Incorporated) white light interferometer with $10 \times$ and $50 \times$ objectives include a $2 \times$ magnifier so that the maximum magnification is $100 \times$.

The vertical resolution claimed by the manufacturer is in the angstrom-range (\sim 1×10⁻¹⁰ m). The vertical resolution was calibrated using a step-height standard. The standard is a quartz slide into which a flat-bottomed "trench" has been manufactured (Very Large Scale Integrated; VSLI). The height difference between the bottom of the trench and the sides is 1.767±0.012 μ m. Repeated measurements yielded a practical detection limit for Δh between the reference and reaction surface of \sim 20 nm.

Upon termination of the experiments the coupons were removed from the reactors and representative images of the corroded surfaces are presented in Figure 14.

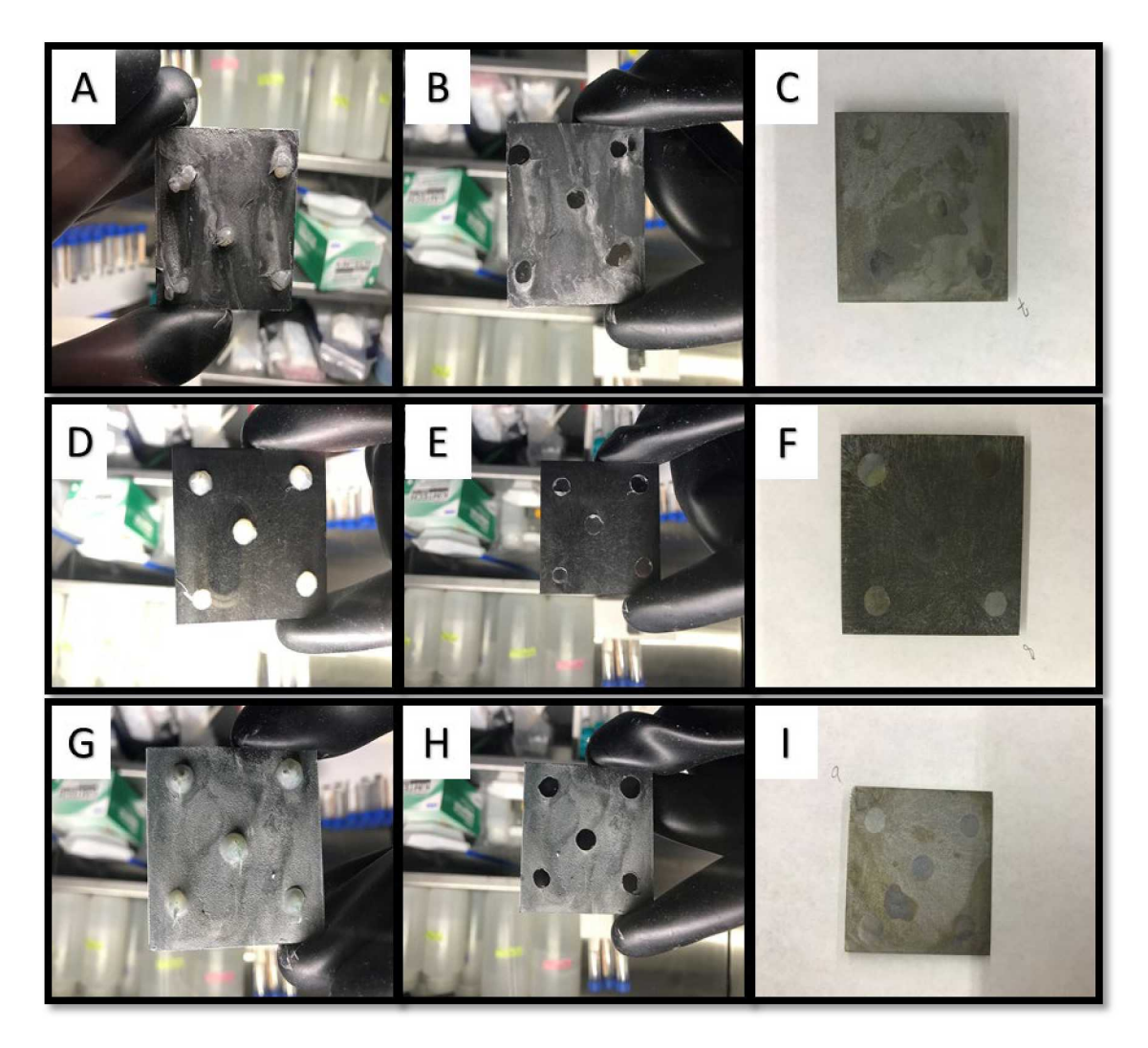


Figure 14. Photographs of post-experiment graphite steel coupons. A. Coupon KIT-F1 (5 M NaCl) before cleaning with silicone mask. B. Coupon KIT-F1 (5 M NaCl) before cleaning with masks removed. C. Coupon KIT-F1 (5 M NaCl) after cleaning. D. Coupon KIT-F2 (3.4 M MgCl₂) before cleaning with silicone masks. E. Coupon KIT-F2 (3.4 M MgCl₂) before cleaning with masks removed. F. Coupon KIT-F2 (3.4 M MgCl₂) after cleaning. G. Coupon KIT-F3 (Soln. 3) before cleaning with masks removed. I. Coupon KIT-F3 (Soln. 3) after cleaning.

Graphite steel coupons reacted in NaCl, MgCl₂ and Solution 3, in general, displayed a thin layer of corrosion products (Figures 14A, 14D, 14G). After removing the corrosion products and cleaning the surface of the coupons, dissolution appears to have accented the striated structure of the steel underlying the polished surface. The areas underlying the RTV masking agent (the reference surface) can be viewed as small, polished irregularly shaped circles and ovals. A fraction of the corrosion products was removed for characterization. In contrast, Cr-Ni steel

coupons that were reacted in NaCl, MgCl₂, and solution 3 solutions were covered with dried salt from the brine compositions (Figure 15). Very little or any corrosion occurred as seen in the images after cleaning had occurred. Images of the cleaned coupons are exhibited in Figures 15C, 15F, 15I.

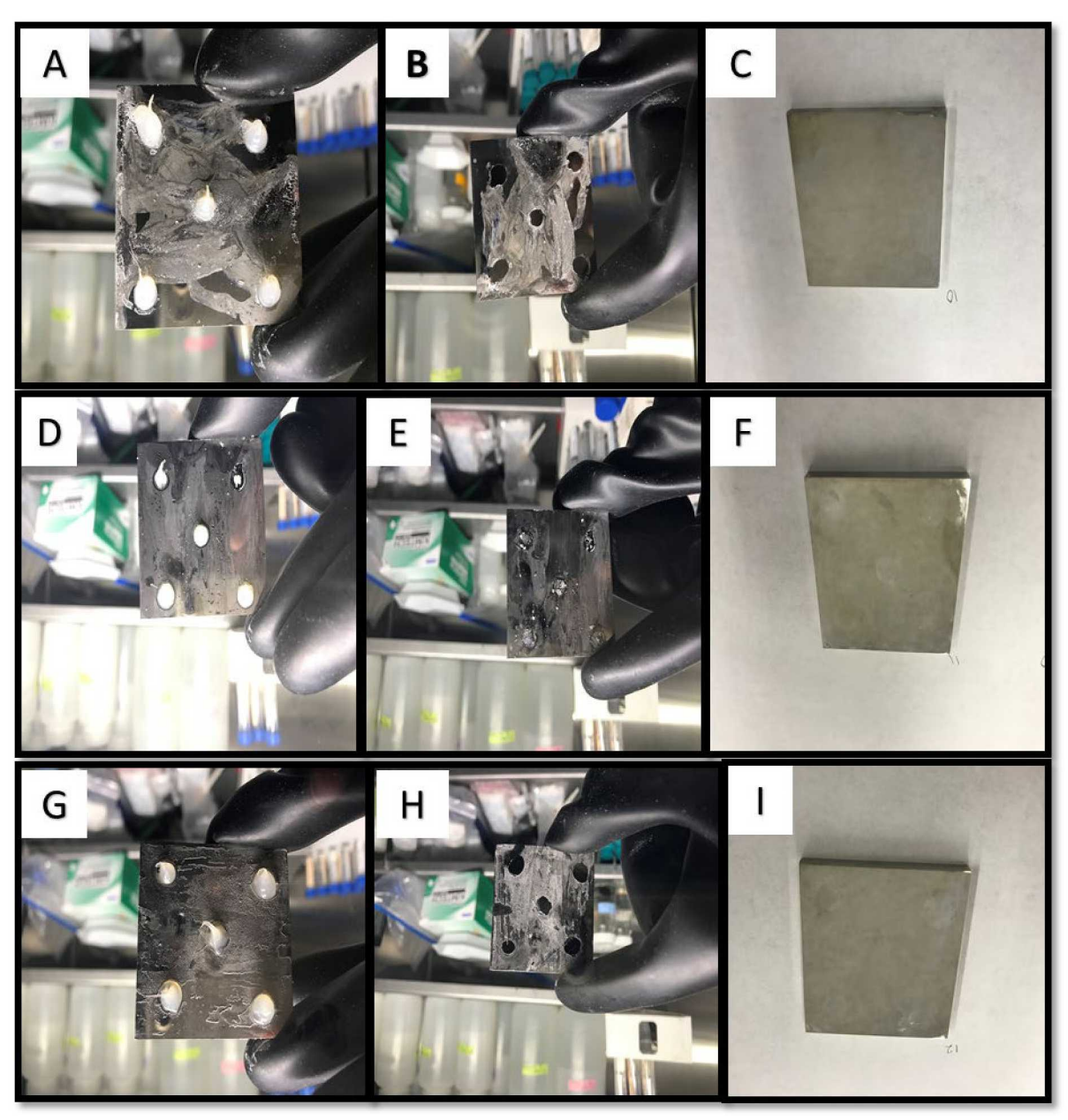


Figure 15. Photographs of post-experiment Cr-Ni steel coupons. A. Coupon KIT-F4 (5 M NaCl) before cleaning with silicone mask. B. Coupon KIT-F4 (5 M NaCl) before cleaning with masks removed. C. Coupon KIT-F4 (5 M NaCl) after cleaning. D. Coupon KIT-F5 (3.4 M MgCl₂) before cleaning with silicone masks. E. Coupon KIT-F5 (3.4 M MgCl₂) before cleaning with masks removed. F. Coupon KIT-F5 (3.4 M MgCl₂) after cleaning. G. Coupon

KIT-F6 (Soln. 3) before cleaning with silicone masks. H. Coupon KIT-F6 (Soln. 3) before cleaning with masks removed. I. Coupon KIT-F6 (Soln. 3) after cleaning.

With the corrosion products removed, the surface retreat could be directly measured by interferometry. An interferometric image of the polished surface of the coupon prior to exposure to solution is displayed in Figures 16. This figure exhibits a camera image of a representative area of the surface. A profile across the polished surface reveals small height differences (34 nm, maximum).

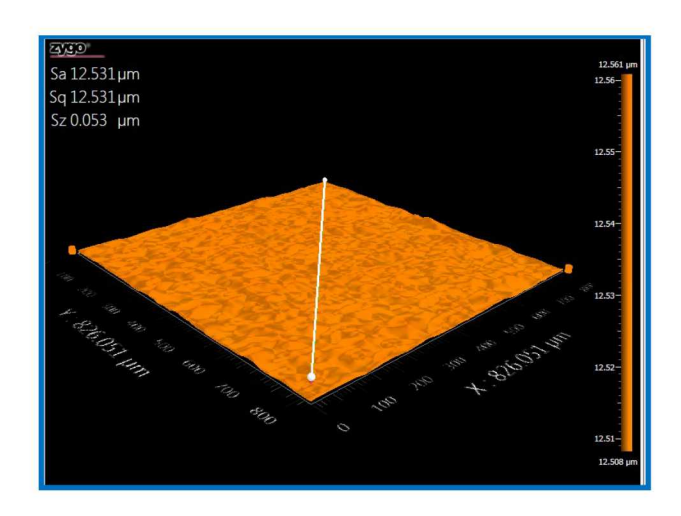


Figure 16. Interferometer image of a polished coupon surface before it was subjected to aqueous corrosion.

Interferometry images were also acquired in areas at the interface between reference and reacted surfaces to display the contrast in relative height between these surfaces. In contrast, the reaction surfaces of graphite steel coupons reacted in NaCl (Figure 17), MgCl₂ (Figure 18), and solution 3 (Figure 19), (after cleaning) display significant surface roughening with maximum height differences between highs and lows of $1-6 \mu m$.

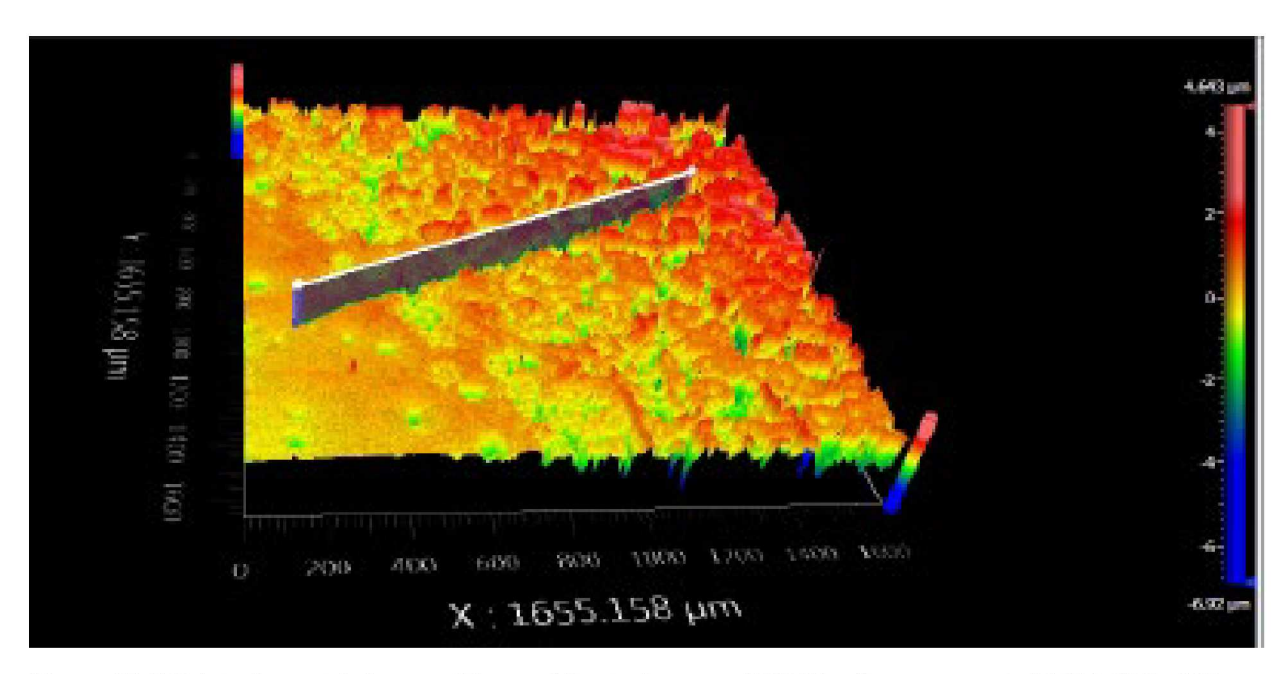


Figure 17. 3-D interferometric image of the graphite steel coupon, KIT-F1, after exposure to 5 M NaCl for 160 days. The surface shows evidence of extensive roughening.

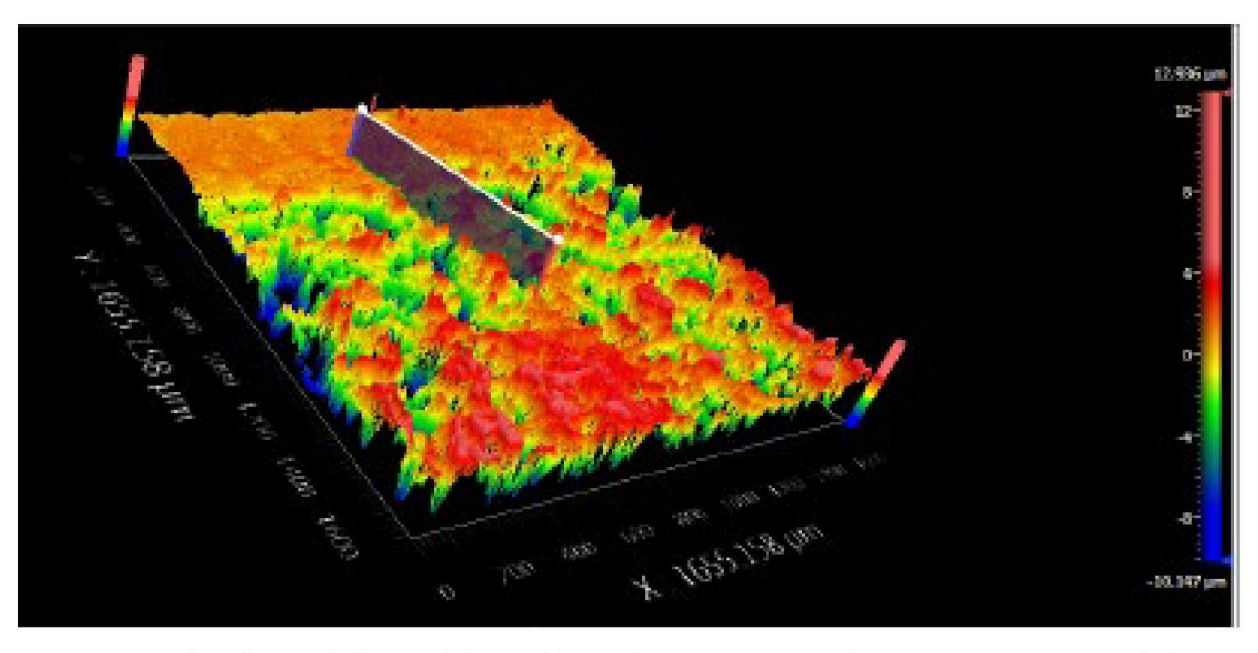


Figure 18. 3-D interferometric image of the graphite steel coupon, KIT-F2, after exposure to 3.4 M MgCl₂ for 160 days. The surface shows evidence of extensive roughening and pitting.

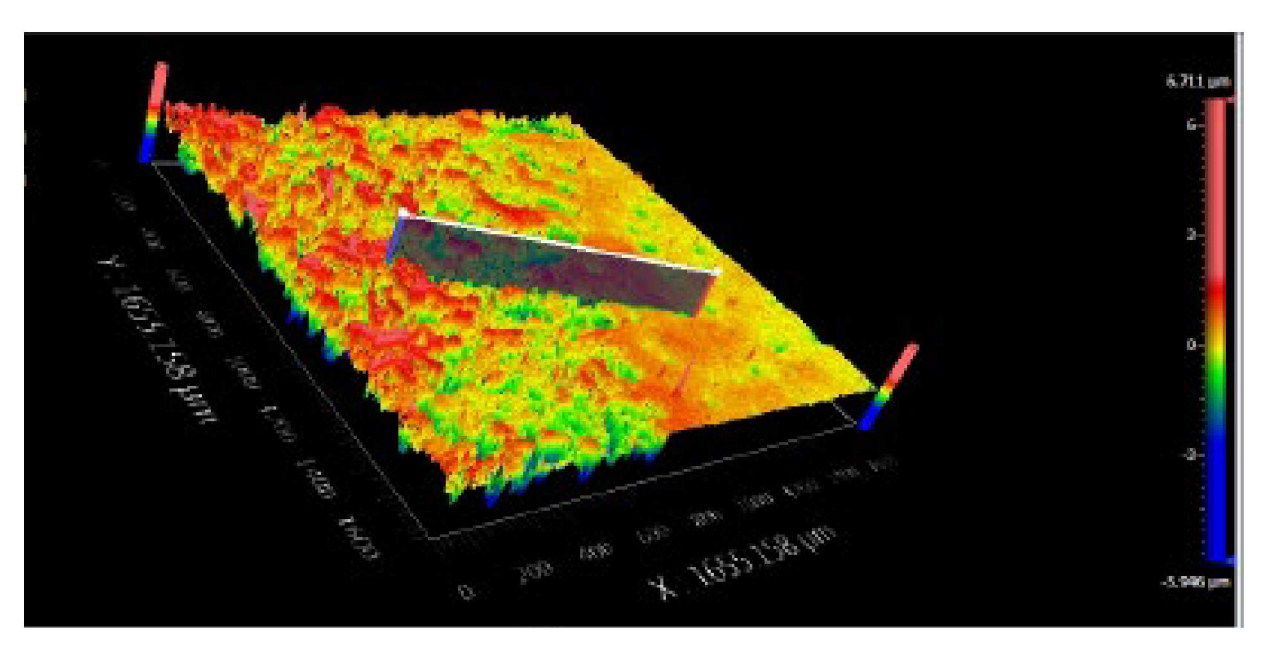


Figure 19. 3-D interferometric image of the graphite steel coupon, KIT-F3, after exposure to Soln. 3 for 160 days. The surface shows evidence of extensive roughening.

As an example, Figure 18 illustrates the difference in relative height between reference and reacted surfaces; the height difference is clear. A profile across the reference surface to the reacted surface reveals a height difference of ~6 µm. To obtain statistically valid measurements of this height difference, the "masking" option in MetroPro, the software that drives image acquisition for the interferometer, was used. The masking option allows the user to select areas on both the reference and reaction surfaces, and the software computes the average height over area chosen. In this way, the average surface height over large areas can be acquired, which is critical for the roughened reaction surface. The software therefore employs the Law of Large numbers in determining the average surface height of the reaction surface.

The height difference between the reference and reaction surfaces for experiments run with graphite steel (KIT-F1, -F2, -F3) is relatively large (>1 µm). Even for graphite steel coupon experiments, in which the dissolution rate was not as fast (KIT-F1 and KIT-F3), the height difference between reference and reaction surfaces was still measurable, Figures 17 and 19. In

experiment KIT-F1, for example, the rate of dissolution appears to be relatively slow, but the 3-D height map reveals that the reference and reaction surfaces can clearly be distinguished from each other by height (Figure 17). In this example, the height difference between the reference and reacted surfaces is \sim 2.4 μ m, well within the resolving power of the interferometer.

Unfortunately, the 3-D height map for the Cr-Ni steel coupons (KIT-F4, -F5, -F6) reported low results with high uncertainties. This is due to the fact that less corrosion occurred, resulting in minimal surface roughness and pitting, as seen in Figures 20-22.

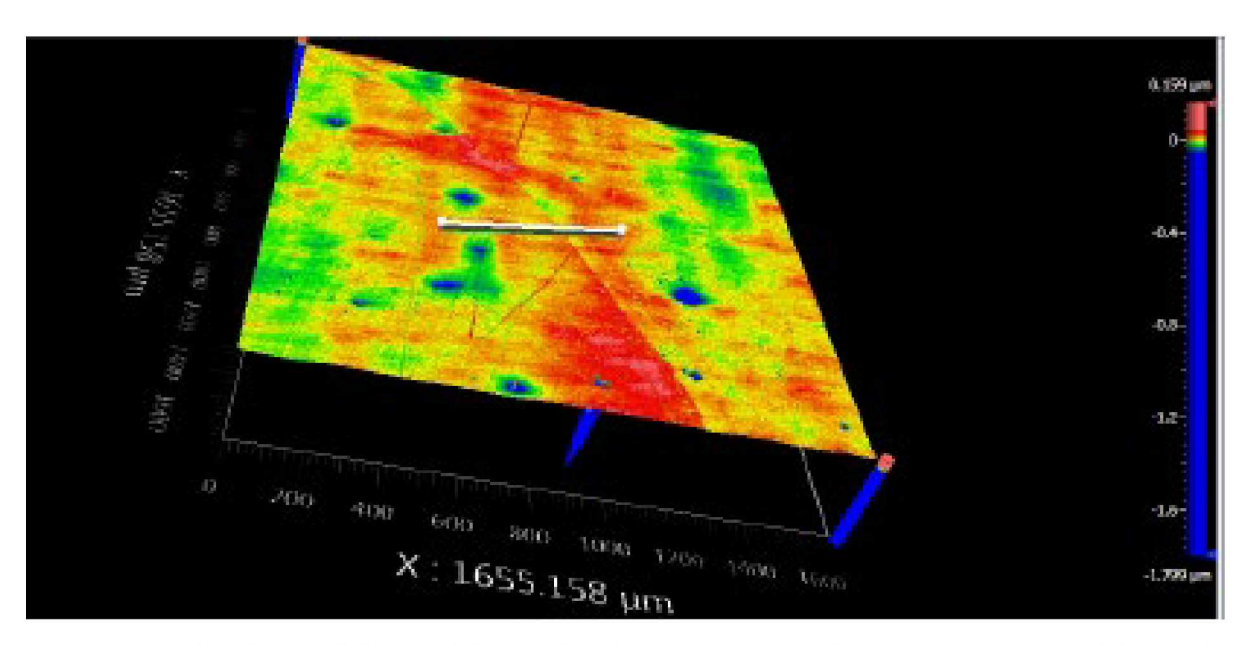


Figure 20. 3-D interferometric image of the Cr-Ni steel coupon, KIT-F4, after exposure to 5 M NaCl for 160 days. The surface shows little evidence of surface roughening.

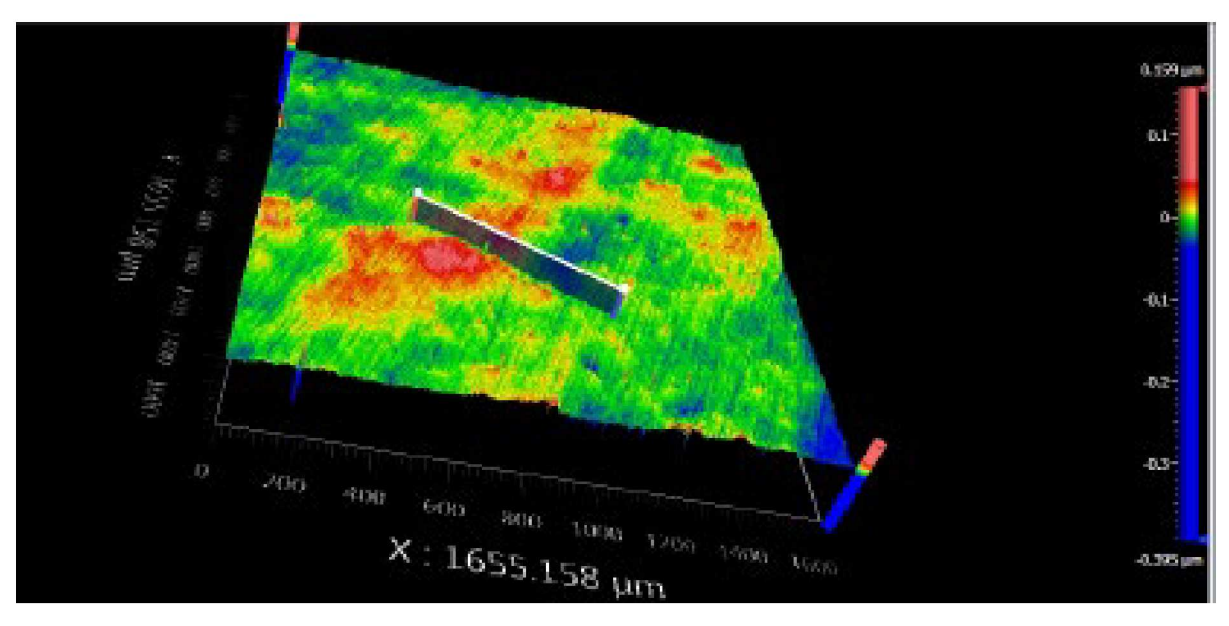


Figure 21. 3-D interferometric image of the Cr-Ni steel coupon, KIT-F5, after exposure to 3.4 M MgCl₂ for 160 days. The surface shows little evidence of surface roughening.

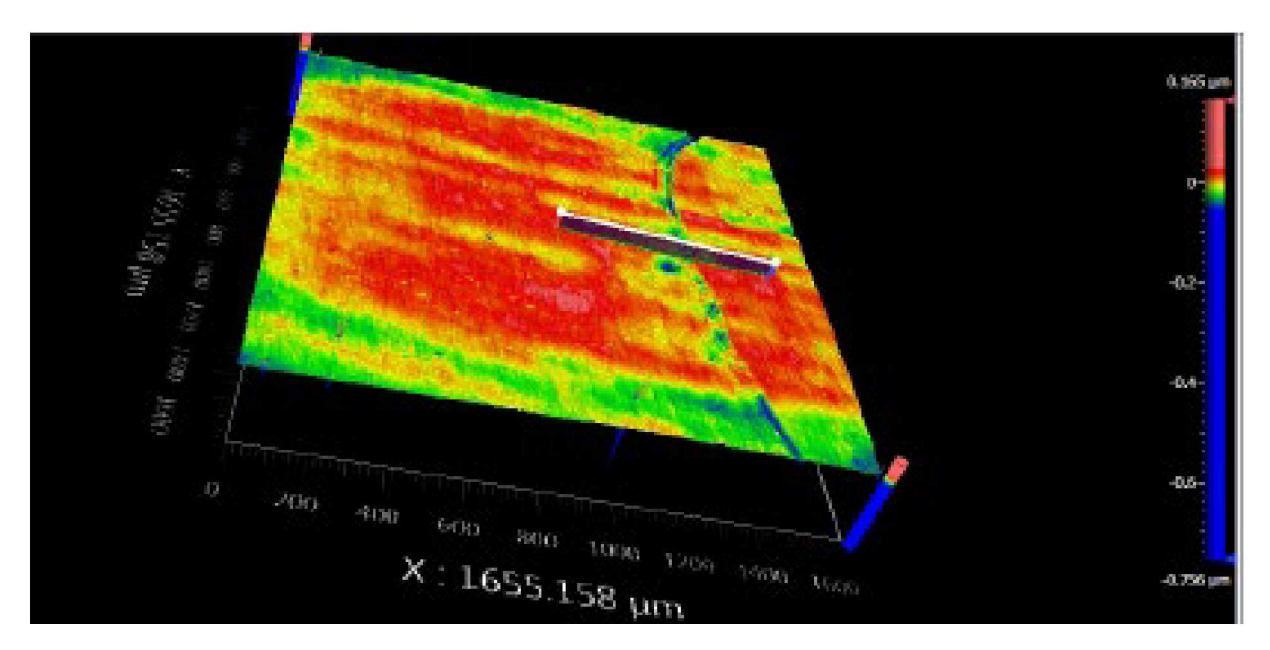


Figure 22. 3-D interferometric image of the Cr-Ni steel coupon, KIT-F6, after exposure to Soln. 3 for 160 days. The surface shows little evidence of surface roughening.

Table 10 lists the data acquired by interferometry on coupons.

Table 10 Interferometer Corrosion Rates for Samples

| Sample ID | Chemical Composition | Brine | Corrosion Rate (µm/yr) | Corrosion Rate (g/(m ² d)) |
|-----------|----------------------|-------------------------|------------------------|---------------------------------------|
| KIT-F1 | Graphite steel | 5.0 M NaCl | 5.42 ± 1.22 | 0.152 ± 0.034 |
| KIT-F2 | Graphite steel | 3.4 M MgCl ₂ | 10.13 ± 2.29 | 0.278 ± 0.063 |
| KIT-F3 | Graphite steel | Solution 3 | 5.00 ± 0.85 | 0.139 ± 0.024 |
| KIT-F4 | Cr-Ni steel | 5.0 M NaCl | 0.17 ± 0.16 | 0.0052 ± 0.0049 |
| KIT-F5 | Cr-Ni steel | 3.4 M MgCl ₂ | 0.31 ± 0.48 | 0.0094 ± 0.0147 |
| KIT-F6 | Cr-Ni steel | Solution 3 | 0.08 ± 0.04 | 0.0023 ± 0.0014 |

The data indicate that surface retreat of steel in MgCl₂ (KIT-F2) for graphite steel is approximately 10 µm/yr. Dissolution rates of graphite steel coupons in NaCl and solution 3 (KIT-F1 and KIT-F3) were 5.4 and 5.0 µm/yr, respectively. The data appear to show that dissolution rates are largely affected by the type of steel used and specifically more so for MgCl₂ bearing solutions. In contrast to this trend, the Cr-Ni coupon dissolved into MgCl₂ solution showed little dissolution. The Cr-Ni coupons (KIT-F4, -F5, -F6) resulted in corrosion rates with high uncertainties associated with them. Due to this, an average of the interferometer results with the mass loss data and total Fe concentration corrosion rates will result in more substantial conclusions.

6.0 Identification of Corrosion Products by Raman Spectroscopy

Ex situ characterization by the Raman spectra were obtained using a Horiba XploRA PLUS visible single spectrometer equipped with a confocal microscope and a Charge Coupled Device (CCD) detector. The 638 nm He-Ne laser was used for excitation. The spectrometer was equipped with a diffraction grating of 1800 lines per mm with a 10x objective lens. Samples for

KIT-F1, -F2, and -F3 were taken by scraping corrosion products from the coupon and placing on a cover slide and then finally being placed in an anoxic sample holder. Samples for KIT-F4, -F5, and -F6 did not result in enough corrosion product to scrape from coupon. Therefore, Raman analysis could not be completed for these samples. Figures 23-25 illustrate the Raman spectra recorded on graphite steel coupon scrapings after the 160 days.

Figure 23 shows the Raman spectra from the graphite steel coupon, sample KIT-F1. The sharpest peak occurs at 665 cm⁻¹. Of the most common iron species, magnetite (Fe₃O₄) exhibits its most intense mode at *ca*. 665 cm⁻¹. This peak is not present in Figure 24 and removes the possibility of the presence of magnetite as a corrosion product for KIT-F2. The Raman spectrum in Figures 23 and 24 show a broad band between 430-500 cm⁻¹ that is characteristic of green rust (GR) compounds (Sabot, 2007). Iron-silica compounds may also be present in the corrosion layer. Other secondary phases such as calcium-silicate hydrates, magnesium silicates, and iron silicates precipitate may also be a possibility. Olivine [(Mg²⁺, Fe²⁺)₂SiO₄], for example, has bands around 820 cm⁻¹ while CaMgSi₂O₆ based glasses by Magnien et al (2006; 2008) observe a band around 915 cm⁻¹.

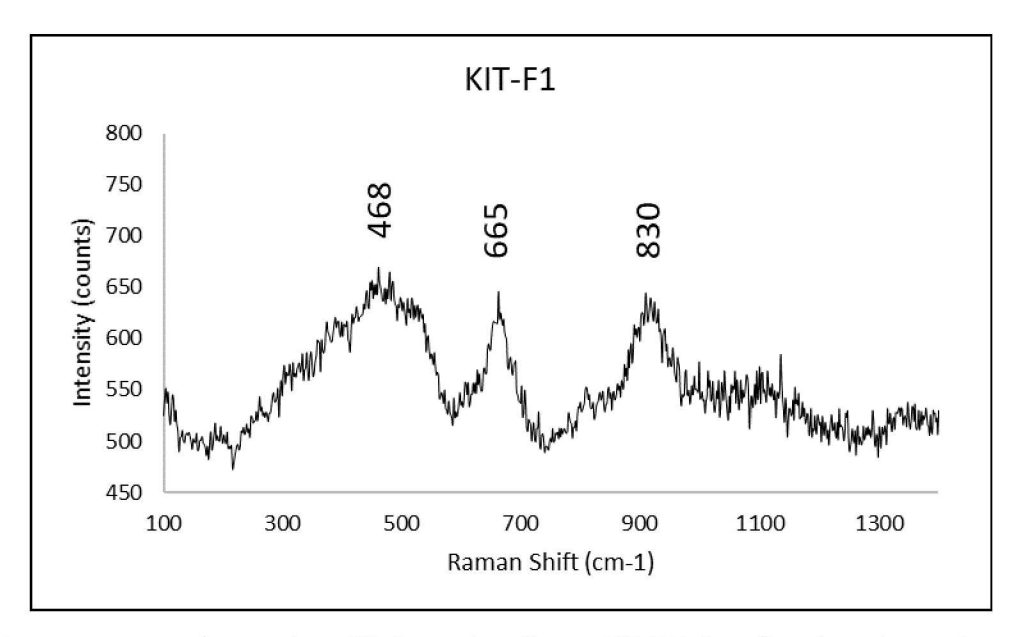


Figure 23. Raman spectrum of magnetite + GR detected on Coupon KIT-F1 from flow through experiments in 5 M NaCl brine.

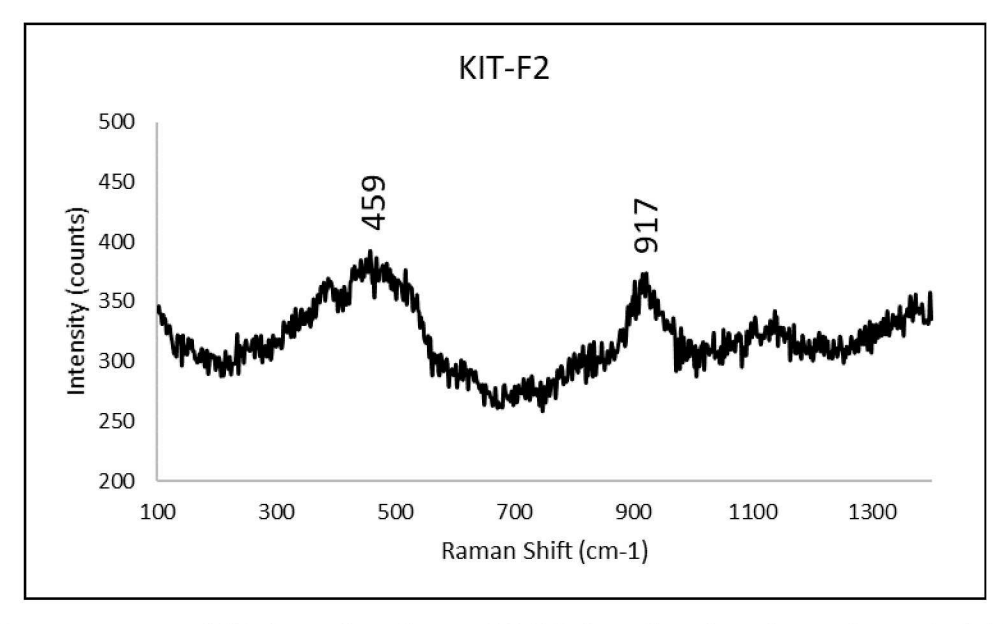


Figure 24. Raman spectrum of GR detected on Coupon KIT-F2 from flow through experiments in 3.4 M MgCl₂ brine.

Akaganeite (β-FeOOH) forms in environments with high chloride concentration (Genin, 1986), and green rust is stable in low-oxygen electrolytes above a certain [Cl⁻]/[OH⁻] ratio (Refait, 2009). Chloride anions are inserted in the c-axis tunnel of the tetragonal lattice of akageneite and contribute to the crystal structure stability (Dasgupta, 1959). The general formula

for green rust is written as (Fe[III]_{1-x}Fe[III]_xOH₂)^{+x} (x/n A · m/nH₂O)^{-x}, where A can be the following anions: Cl⁻¹, SO₄²⁻, CO₂²⁻, SO₃²⁻, OH⁻ (Genin, 1996). Green rust is a precursor to akageneite, as akaganeite precipitates from chlorine-containing green rust (GR1[Cl⁻]) (Refait, 1997). Therefore, the green rust found on the coupon KIT-F3 submerged in solution 3 was most likely GR1(Cl⁻). Figure 25 shows the spectrum from a region that was dominated by green rust because the peak at 420 cm⁻¹ is close to that reported previously for green rust (Refait, 2009). A second region exhibited peaks at 125 and 159 cm⁻¹, Figure 25. These peaks are associated with akageneite and are presumed to be an intermediate compound that formed as green rust transitioned to akageneite. The sharp peaks are not referenced in literature because their characteristic peaks are below 200 cm⁻¹, which is below the spectral range of most commercial Raman spectrometers. The peak at 317 cm⁻¹ is attributed to akageneite, whereas the 620 and 807 cm⁻¹ peaks are attributed to goethite (α-FeOOH).

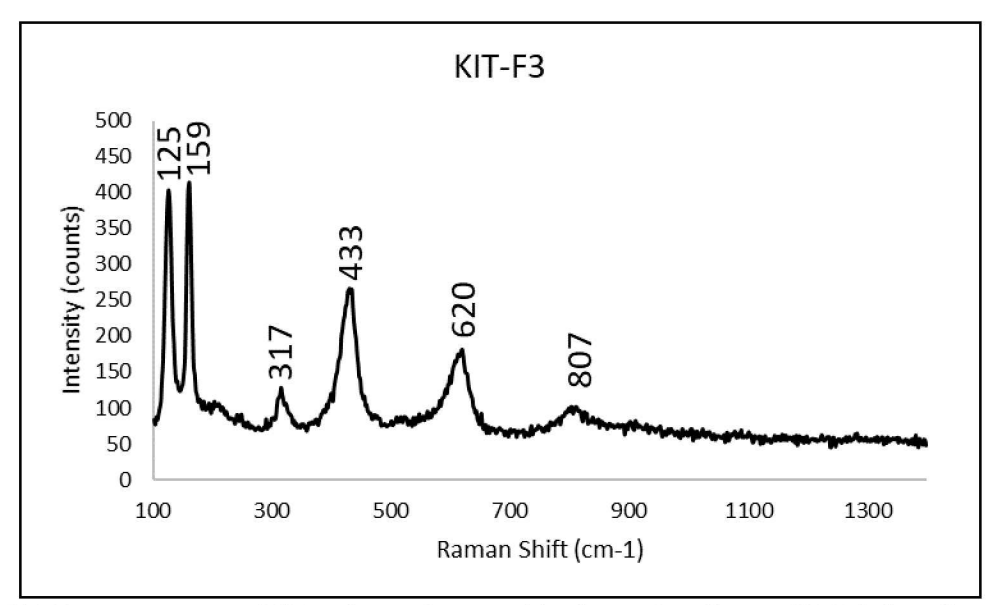


Figure 25. Raman spectrum of GR + akageneite + goethite detected on Coupon KIT-F3 from flow through experiments in Solution 3 brine.

7.0 Uncertainty Determination

In addition to determining the corrosion rate, it is essential to correlate the measurements with uncertainties and understand how uncertainties in measurements affect the calculated corrosion rate in a controlled environment. The examples provided herein impart the guidelines on uncertainties of measurements, where the surface area of a coupon is well defined and consistent for each test. This section calculates uncertainties, assuming errors obey a normal distribution, caused by the measurement of time, mass, and surface area in reference to SPFT experiments at 90°C.

The 1-sigma uncertainties, σ_f , of a continuous function, f, with variables $x_1, x_2, \dots x_n$ can be determined by applying the formula:

$$\sigma_f^2 = \sum_{n=1}^n \left(\frac{\partial f}{\partial x_n}\right)^2 \sigma_{x_n}^2$$
 [4]

where σ_{x_n} is the uncertainty on the n^{th} variable. From Eq. [2], r is a function (f) of W, SA, t, and ρ ; therefore Eq. [4] can be expanded to Eq. [5]:

$$\sigma_r^2 = \left(\frac{\partial r}{\partial W}\right)^2 \sigma_W^2 + \left(\frac{\partial r}{\partial SA}\right)^2 \sigma_{SA}^2 + \left(\frac{\partial r}{\partial t}\right)^2 \sigma_t^2 + \left(\frac{\partial r}{\partial \rho}\right)^2 \sigma_\rho^2$$
 [5]

where r, σ_W , σ_{SA} , σ_t and σ_ρ are, respectively, the rate, uncertainties on the mass, surface area, elapsed time and density. Derivation of Eq. 4 requires evaluating the derivative in Eq. 5 with respect to each variable:

$$\left(\frac{\partial r}{\partial W}\right) = \left(\frac{1000x87.6}{SA \cdot t \cdot \rho}\right), \ \left(\frac{\partial r}{\partial SA}\right) = \left(\frac{-1000Wx87.6}{SA^2 \cdot t \cdot \rho}\right), \ \left(\frac{\partial r}{\partial t}\right) = \left(\frac{-1000Wx87.6}{SA \cdot t^2 \cdot \rho}\right), \ \text{and} \ \left(\frac{\partial r}{\partial \rho}\right) = \left(\frac{-1000Wx87.6}{SA \cdot t \cdot \rho^2}\right)$$

Therefore:

$$\sigma_{r}^{2} = \left(\frac{1000x87.6}{SA \cdot t \cdot \rho}\right)^{2} \sigma_{W}^{2} + \left(\frac{-1000Wx87.6}{SA^{2} \cdot t \cdot \rho}\right)^{2} \sigma_{SA}^{2} + \left(\frac{-1000Wx87.6}{SA \cdot t^{2} \cdot \rho}\right)^{2} \sigma_{t}^{2} + \left(\frac{-1000Wx87.6}{SA \cdot t \cdot \rho^{2}}\right)^{2} \sigma_{\rho}^{2}$$
[7]

Division of Eq. 6 by the square of Eq. 2, produces:

$$\left(\frac{\sigma_r}{r}\right)^2 = \frac{\left(\frac{1}{SA \cdot t \cdot \rho}\right)^2 \sigma_W^2 + \left(\frac{-W}{SA^2 \cdot t \cdot \rho}\right)^2 \sigma_{SA}^2 + \left(\frac{-W}{SA \cdot t^2 \cdot \rho}\right)^2 \sigma_t^2 + \left(\frac{-W}{SA \cdot t \cdot \rho^2}\right)^2 \sigma_\rho^2}{\left(\frac{W}{SA \cdot t \cdot \rho}\right)^2}$$
[8]

For this report $2-\sigma$ uncertainties are reported.

The uncertainty on surface retreat from interferometry (Eq. 3) is:

$$\left(\frac{\sigma_r}{r}\right)^2 = \left\{ \left(\frac{\sigma_\rho}{\rho}\right)^2 + \left(\frac{\sigma_{\Delta h}}{\Delta h}\right)^2 + \left(\frac{\sigma_{\Delta t}}{\Delta t}\right)^2 \right\}$$
 [9]

The uncertainties for density (ρ) , and elapsed time (Δt) are 3% and 1%, respectively. The size of the uncertainty for Δh depends on how close the measured height difference is to the practical uncertainty of 20 nm. For example, if the measured height difference is 350 nm, the uncertainty would be 20/350 nm or 5.7%. However, if the measured height difference was 60 nm, the uncertainty would now be 20/60 nm or 33%. The standard deviation of the Δh value, based on a statistically valid number of interferometer measurements, is typically larger than the 2- σ error computed using [8]. Therefore, the standard deviation on Δh is the more conservative error estimate and is the uncertainty reported in this report.

The error reported for the rate based on Fe release (Eq. 1) is slightly more complicated and utilizes converting the uncertainties into relative standard deviations $(\frac{\sigma_r}{r})$:

$$\hat{\sigma}_{r} = \sqrt{\frac{\left(\hat{\sigma}_{c}c_{Fe}^{out}\right)^{2} + \left(\hat{\sigma}_{c,b}c_{Fe,b}^{in}\right)^{2}}{\left(c_{Fe}^{out} - c_{Fe,b}^{in}\right)^{2}} + \left(\hat{\sigma}_{f_{Fe}}\right)^{2} + \left(\hat{\sigma}_{SA}\right)^{2} + \left(\hat{\sigma}_{Q}\right)^{2}}$$
[10]

where $\hat{\sigma}_C$, $\hat{\sigma}_{C,b}$, $\hat{\sigma}_{f_{Fe}}$, $\hat{\sigma}_{SA}$ and $\hat{\sigma}_Q$ are the relative uncertainties on the concentration of iron, the background concentration of iron, the mass fraction of Fe in the steel monolith and the flow-rate, respectively.

8.0 Conclusions

Experimental results obtained by the SPFT test indicate that MgCl₂ is more corrosive than NaCl and solution 3 to the graphite steel coupons tested. The rate of corrosion varies from metal to metal. For graphite steel coupons, the average corrosion rate caused by MgCl₂ is 3 to 5 times higher than by NaCl and solution 3 (Figure 26); for Cr-Ni coupons, the average corrosion rate caused by MgCl₂ is similar to solution 3 brine (Figure 27), within uncertainty. Two factors may lead to the higher corrosion rate of MgCl₂ for the graphite steel coupons. One is its lower pH value, and the other is its higher chloride concentration in the solution, compared to NaCl of the similar weight percentage concentration. The measured pH-values in the NaCl-rich, MgCl₂-rich, and sulfate-rich brines was between 8.4 to 9.1, 6.3 to 7.8, and 7.6 to 8.8, respectively, at room temperature. All brines experienced a very slow increase in pH throughout the 23-week experiments at 90 °C.

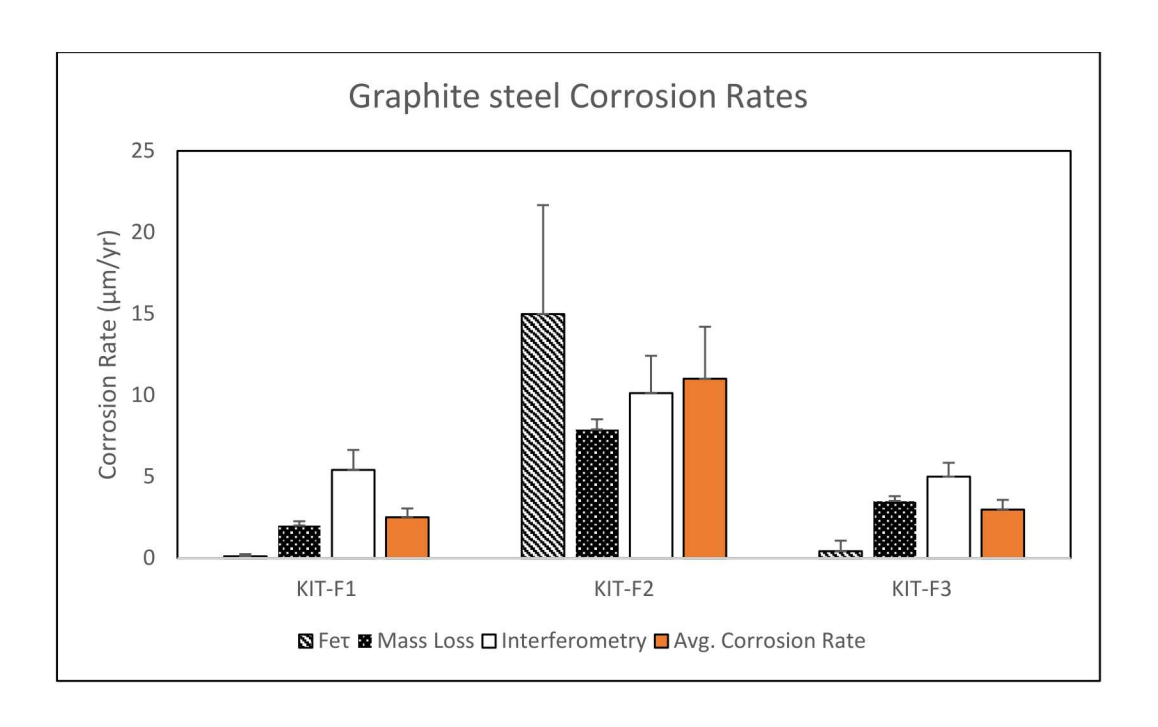


Figure 26. Graphite steel coupon corrosion rates using Total iron (Fe $_{\tau}$), mass loss, and interferometry techniques.

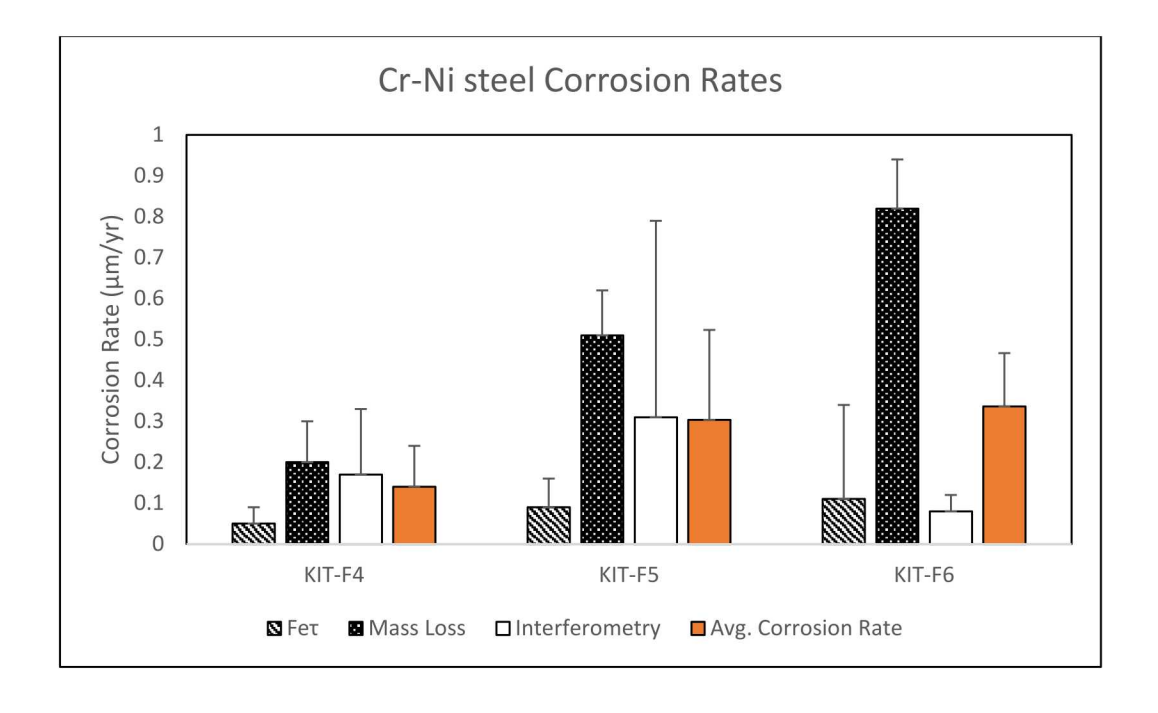


Figure 27. Cr-Ni steel coupon corrosion rates using Total iron (Fe $_{\tau}$), mass loss, and interferometry techniques.

With approximately the same concentration level, the MgCl₂ solution has lower pH values than the NaCl solution. This is because MgCl₂ can hydrolyze according to MgCl₂+ H₂O \rightarrow Mg(OH)Cl + HCl (Silcock, 1979). This means there are more hydrogen ions in the corrosion medium when MgCl₂ is used as the solute. The hydrogen ions can interact and modify the surface and therefore alter the corrosion resistance of the material. Moreover, interactions between pH and dissolved species such as chloride ions can enhance the effect of hydrogen ions. Consequently, the metals subjected to the MgCl₂ solution have a higher corrosion rate. Chloride ions do not chemically react with the metals. Chloride ions only assume a role as a medium or catalyst in the corrosion process. Chloride anions in the solution could help to remove the metal cations accumulated by forming soluble compounds, and this contributes to an accelerated anodic reaction and thus faster rusting of the metals. This hypothesis is supported by the research of Ambat and Dwarakadasa (1993), who found the concentration of chloride had great effect on the corrosion rate of steel alloys in the region of neutral pH. They considered that the strong dependence of the corrosion rate of iron on chloride ion concentration in a neutral environment might be explained by taking into account the adherent oxide film that is present on the surface of the alloy. In such cases, the presence of chloride ions can accelerate the corrosion by retarding film repair. At the film/solution interface, chloride ions lead to a local thinning of the passive layer and to pitting corrosion.

Table 11 Average corrosion rates for KIT graphite steel and Cr-Ni steel coupons based on Fe_{τ} , mass loss, and interferometry results.

| Sample ID | Chemical Composition | Brine | Avg. Corrosion Rate (μm/yr) |
|-----------|-------------------------|-------------------------|-----------------------------|
| KIT-F1 | Graphite steel | 5.0 M NaCl | 2.51 ± 0.54 |
| KIT-F2 | Graphite steel | 3.4 M MgCl ₂ | 11.00 ± 3.20 |
| KIT-F3 | Graphite steel | Solution 3 | 2.98 ± 0.59 |
| KIT-F4 | Cr-Ni steel | 5.0 M NaCl | 0.14 ± 0.10 |
| KIT-F5 | Cr-Ni steel | 3.4 M MgCl ₂ | 0.30 ± 0.22 |
| KIT-F6 | Cr-Ni steel | Solution 3 | 0.34 ± 0.13 |

Since the oxide film on the surface of the iron is soluble in both low and high pH solutions, the change of pH has a great influence on iron corrosion. This influence is profound because the solutions of NaCl and $MgCl_2$ have different pH values even with same weight percentage concentration.

The present work and calculations (Sisk-Scott, 2019a) combining classical weight loss measurements, total iron concentration, and 3-D interferometry with the identification of fine corrosion products with Raman spectroscopy, leads us to conclude that the concentration of aqueous chloride, type of metal, and the structural properties of the corrosion products are determinant factors in the inhibition of steel corrosion under anaerobic conditions.

9.0 References

- Ambat, R. and Dwarakadasa, E.S., Effects of chloride ion concentration during corrosion of medium strength aluminum alloys 8090, 2091, and 2014, *British Corrosion Journal*, Vol. 28, no. 2, (1993): p. 142-148.Crovisier, J. L., Advocat, T. & Dussossoy, J. L. Nature and role of natural alteration gels formed on the surface of ancient volcanic glasses (Natural analogs of waste containment glasses). *J. Nucl. Mater.* 321, 91–109 (2003).
- Cruz, R.P.V., Nishkata, A., Tsuru, T., Pitting corrosion mechanism of stainless steels under wetdry exposure in chloride-containing environments. Corrosion Science, 40 (1998): p. 125-139.
- Dasgupta, D.R., Mackay, A.L., β-Ferric oxyhydroxide and green rust. *J. Phys. Soc. Jpn.* 14 (1959): p. 932-935.
- Genin, J.M.R., Olowe, A. A., Refait, Simon, P., L., On the stoichiometry and Pourbaix diagram of Fe (II)-Fe (III) hydroxy-sulphate or sulphate-containing green rust 2: an electrochemical and Mössbauer spectroscopy study, Corros. Sci. 38 (1996): p. 1751-1762.
- Genin, J.M., Bauer, P., Olowe, A.A., Rezel, D., Mössbauer study of the kinetics of simulated corrosion process of iron in chlorinated aqueous solution around room temperature: The hyperfine structure of ferrous hydroxides and Green Rust I, *Hyperfine Interact*. 29 (1986): p. 1355-1360.
- Icenhower, J. P. and Steefel, C. I. (2015) Dissolution rate of borosilicate glass SON68: A method of quantification based upon interferometry and implications for experimental and natural weathering rates of glass. Geochimica et Cosmochimica Acta 157, 147-163.
- Magnien, V., Neuville, D.R., Cormier, L., Roux J., Hazemann, J-L., Pinet, O., Richet, P., 2006. Kinetics of iron redox reactions in silicate liquids: A hightemperature X-ray absorption and Raman spectroscopy study. J. Nucl. Mat., 352, 190-195.
- Magnien, V., Neuville D.R., Cormier L., Roux J., Hazemann J-L., de Ligny D., Pascarelli S., Vickridge I., Pinet O., Richet P., 2008. Kinetics and mechanisms of iron redox reactions

- in silicate melts: The effects of temperature and alkali cations. Geochim. Cosmochim. Acta. (in press).
- Refait, P., Nguyen, D.D, Jeannin, M., Sable, S., Langumier, M., Sabot, R., *Electrochim. Acta* 56 (2011): p. 6481-6488.
- Refait, P., Genin, J.M.R., The mechanisms of oxidation of ferrous hydroxychloride β-Fe2 (OH) 3Cl in aqueous solution: the formation of akaganeite vs goethite, *Corros. Sci.* 39 (1997): p. 539-553.
- Refait, P., Girault, P., Jeannin, M., J. Rose, Influence of arsenate species on the formation of Fe(III) oxyhydroxides and Fe(II–III) hydroxychloride, *Colloids Surf.*, A 332 (2009): p. 26-35.
- Sabot, R., Jeannin, M., Gadouleau, M., Guo, Q., Sicre, E., Refait, Ph., Influence of lactate ions on the formation of rust, Corros. Sci. 49 (2007) 1610–1624.
- Silcock, J.M., "Effect of acidity and applied potential on the stress corrosion cracking of type 316 austenitic steel in MgCl₂, *British Corrosion Journal*. Vol. 14, No. 4, (1979): p. 206-215.
- Sisk-Scott, C., Iron and lead corrosion in WIPP-relevant conditions: Static and solution flow-through corrosion experiments milestone report. September 2019. ERMS 572066. Sandia National Laboratories, Carlsbad, NM.
- Sisk-Scott, C., *KIT_Weeks 1-22_100119.xlsx* Excel spreadsheet, located at /nfs/data/CVSLIB/WIPP_EXTERNAL/KIT, (2019a). Sandia National Laboratories, Carlsbad, NM.
- Sisk-Scott, C., Icenhower, J., Iron and lead corrosion in WIPP-relevant conditions Test Plan TP 06-02, Rev. 3, January 2016. ERMS 565448. Sandia National Laboratories, Carlsbad, NM.

Sandia National Laboratories is a multi-mission laboratory managed and operated by National Technology and Engineering Solutions of Sandia, LLC., a wholly owned subsidiary of Honeywell International, Inc., for the U.S. Department of Energy's National Nuclear Security Administration under contract DE-NA-0003525. This research is funded by WIPP programs administered by the Office of Environmental Management (EM) of the U.S. Department of Energy.